

ODIN: A New Lyman Alpha Blob Selection Method, Sample, and Statistical Analysis at $z \sim 3.1$

BYEONGHA MOON ^{1,2} YUJIN YANG ^{1,2} KYOUNG-SOO LEE ³ ERIC GAWISER ⁴ ARJUN DEY ⁵
FRANCISCO VALDES ⁶ DUSTIN LANG ^{7,8} ROBIN CIARDULLO ^{9,10} CARYL GRONWALL ^{9,10} ANN ZABLUDOFF ¹¹
VANDANA RAMAKRISHNAN ³ NICOLE M. FIRESTONE ⁴ ETHAN PINARSKI ³ SEOK-JUN CHANG ¹²
LUCIA GUAITA ^{13,14} SUNGRYONG HONG ¹ HO SEONG HWANG ^{15,16} SANG HYEOK IM ^{15,17}
WOONG-SEOB JEONG ^{1,2} EUNSOO JUN ^{1,2} SEONGJAE KIM ^{1,2} JAEHYUN LEE ¹ SEONG-KOOK LEE ^{15,16}
GAUTAM NAGARAJ ¹⁸ JULIE B. NANTAIS ¹⁹ NELSON PADILLA ²⁰ CHANGBOM PARK ¹⁷ HYUNMI SONG ²¹ AND
PAULINA TRONCOSO ²²

¹Korea Astronomy and Space Science Institute, 776 Daedeokdae-ro, Yuseong-gu, Daejeon, Korea 34055

²Korea National University of Science and Technology, Daejeon, Korea 34113

³Department of Physics and Astronomy, Purdue University, 525 Northwestern Avenue, West Lafayette, IN 47907, USA

⁴Department of Physics and Astronomy, Rutgers, the State University of New Jersey, Piscataway, NJ 08854, USA

⁵NSF's NOIRLab, 950 N. Cherry Ave., Tucson, AZ 85719, USA

⁶National Optical Astronomy Observatory, 950 N. Cherry Avenue, Tucson, AZ 85719, USA

⁷Perimeter Institute for Theoretical Physics, 31 Caroline Street North, Waterloo, ON N2L 2Y5, Canada

⁸Department of Physics and Astronomy, University of Waterloo, Waterloo, ON N2L 3G1, Canada

⁹Department of Astronomy & Astrophysics, The Pennsylvania State University, University Park, PA 16802, USA

¹⁰Institute for Gravitation and the Cosmos, The Pennsylvania State University, University Park, PA 16802, USA

¹¹Astronomy Department and Steward Observatory, University of Arizona, 933 North Cherry Avenue, Tucson, Arizona, 85721, USA

¹²Max-Planck-Institut für Astrophysik, Karl-Schwarzschild-Straße 1, 85748 Garching b. München, Germany

¹³Universidad Andres Bello, Facultad de Ciencias Exactas, Departamento de Física y Astronomía, Instituto de Astrofísica, Fernandez Concha 700, Las Condes, Santiago RM, Chile

¹⁴Millennium Nucleus for Galaxies (MINGAL)

¹⁵Astronomy Program, Department of Physics and Astronomy, Seoul National University, 1 Gwanak-ro, Gwanak-gu, Seoul 08826, Republic of Korea

¹⁶SNU Astronomy Research Center, Seoul National University, 1 Gwanak-ro, Gwanak-gu, Seoul 08826, Republic of Korea

¹⁷Korea Institute for Advanced Study, 85 Hoegi-ro, Dongdaemun-gu, Seoul 02455, Republic of Korea

¹⁸Laboratoire d'Astrophysique, EPFL, 1015 Lausanne, Switzerland

¹⁹Facultad de Ciencias Exactas, Departamento de Física y Astronomía, Instituto de Astrofísica, Universidad Andrés Bello, Fernández Concha 700, Edificio C-1, Piso 3, Las Condes, Santiago, Chile

²⁰Instituto de Astronomía Teórica y Experimental, CONICET-Universidad Nacional de Córdoba, Laprida 854, X5000BGR, Córdoba, Argentina

²¹Department of Astronomy and Space Science, Chungnam National University, 99 Daehak-ro, Yuseong-gu, Daejeon, 34134, Republic of Korea

²²Escuela de Ingeniería, Universidad Central de Chile, Avenida Francisco de Aguirre 0405, 171-0614 La Serena, Coquimbo, Chile

ABSTRACT

Ly α blobs (LABs) are large, spatially extended Ly α -emitting objects whose nature remains unclear. Their statistical properties such as number densities and luminosity functions are still uncertain because of small sample sizes and large cosmic variance. The One-hundred-deg² DECam Imaging in Narrowbands (ODIN) survey, with its large volume, offers an opportunity to overcome these limitations. We describe our LAB selection method and present 112 new LABs in the 9 deg² E-COSMOS field. We begin with the conventional LAB selection approach, cross-matching LAEs with extended Ly α sources, yielding 89 LAB candidates. To obtain a more complete LAB sample, we introduce a new selection pipeline that models all galaxies detected in deep broadband imaging, subtracts them from the narrowband image, and then directly detects extended Ly α emission. This method successfully identifies 23 additional low-surface-brightness LABs which could otherwise be missed by the conventional method. The number density of ODIN LABs near an ODIN protocluster ($n = 7.5 \times 10^{-5}$ cMpc⁻³) is comparable to that found in the SSA22 proto-cluster and is four times higher than the average across the field. The cumulative Ly α luminosity function within the protocluster regions is

similar to that measured for the LABs in the SSA22 proto-cluster, suggesting a large excess of luminous LABs relative to the average field. These findings suggest the Ly α luminosities and number densities of LABs are environment-dependent. ODIN will provide an expansive LAB and protocluster samples across six additional fields and two more redshifts, allowing us to investigate the nature of LABs in relation to their environments.

Keywords: Galaxies (573) — Intergalactic medium (813) — Lyman-alpha galaxies (978) — Circumgalactic medium (1879) — High-redshift galaxy clusters (2007)

1. INTRODUCTION

Ly α blobs (LABs or “nebulae”) are extended halos of Ly α emitting gas at $z \sim 2\text{--}6$ that are typically $\gtrsim 5''$ ($\gtrsim 50$ pkpc) with line luminosities of $L_{\text{Ly}\alpha} \gtrsim 10^{43}$ erg s $^{-1}$ (W. C. Keel et al. 1999; C. C. Steidel et al. 2000; P. J. Francis et al. 2001; P. Palunas et al. 2004; Y. Matsuda et al. 2004; A. Dey et al. 2005; T. Saito et al. 2006; Y. Yang et al. 2009, 2010; D. K. Erb et al. 2011; M. Li et al. 2024). Originally introduced by C. C. Steidel et al. (2000) to describe extended Ly α -emitting objects lacking obvious AGN or UV continuum sources, the term “LAB” is now widely used to refer to spatially extended Ly α sources with characteristic luminosity and sizes described above. In this work, we adopt the broader definition.

More generally, extended Ly α emitting objects have a wide range of sizes and luminosities (M. Ouchi et al. 2020, for a review). Ly α halos (LAHs) surrounding identifiable galaxies have Ly α luminosities of $L_{\text{Ly}\alpha} \lesssim 10^{43}$ erg s $^{-1}$ and smaller sizes (< 30 pkpc). LAHs are thought to be powered not only by star formation, but also by mechanisms such as gas cooling and fluorescence (R. Mose et al. 2016; F. Leclercq et al. 2017; H. Kusakabe et al. 2022). On the brighter end, enormous Ly α nebulae reach $L_{\text{Ly}\alpha} \sim 10^{45}$ erg s $^{-1}$ and are illuminated by QSOs (S. Cantalupo et al. 2014; J. F. Hennawi et al. 2015; Z. Cai et al. 2017; F. Arrigoni Battaia et al. 2018).

The nature of LABs, which lie between these two extremes, is not well understood. Several mechanisms have been proposed to explain their formation, potentially acting together: star-formation within embedded galaxies (J. E. Geach et al. 2016; Y. Kato et al. 2018) photoionization by AGNs (A. Dey et al. 2005; J. E. Geach et al. 2009; Y. Yang et al. 2014), and gravitational cooling (J. Rosdahl & J. Blaizot 2012; Y. Ao et al. 2020; E. Daddi et al. 2021; F. Arrigoni Battaia et al. 2022). Resonant scattering may play an important role in the extent of Ly α emission (M. Hayes et al. 2011; C. You et al. 2017; E. Kim et al. 2020).

LABs appear to be closely tied to their environments, e.g., overdensities of compact Ly α emitting galaxies (LAEs) (Y. Matsuda et al. 2004, 2011; Y. Yang et al. 2010; M. K. M. Prescott et al. 2008, 2012b; S. Kikuta et al. 2019; H. Zhang et al. 2025). For example, T. Bădescu et al. (2017) has shown that LABs often reside on the outskirts of LAE overdensities, which suggests

that LABs trace infalling substructures or protogroups and that the extended Ly α emitting gas represents a proto-intragroup medium and/or gas stripped through galaxy interactions. D. K. Erb et al. (2011) report an potential alignment of LABs along large-scale filaments in the HS1700 protocluster at $z = 2.3$. More recently, H. Umehata et al. (2019) and V. Ramakrishnan et al. (2023) demonstrate that LABs live in and near cosmic filaments. Because of their link to large-scale structure, their complex nature, and their extensive gaseous halos, LABs are laboratories for studying hierarchical structure formation and the interplay between galaxies and the circumgalactic medium (CGM) and intergalactic medium (IGM).

To date, many LABs have been discovered through narrowband surveys with a variety of filters ($2 < z < 7$), survey fields, surface brightness limits and survey areas (P. J. Francis et al. 2001; P. Palunas et al. 2004; Y. Matsuda et al. 2004, 2011; T. Saito et al. 2006; Y. Yang et al. 2009, 2010; D. K. Erb et al. 2011; T. Shibuya et al. 2018; S. Kikuta et al. 2019; H. Zhang et al. 2020; M. Li et al. 2024). Because LABs are rare and exhibit strong field-to-field variation (Y. Yang et al. 2010), their statistical properties—such as number densities, luminosity functions, clustering properties—remain poorly constrained (e.g., T. Saito et al. 2006; T. Shibuya et al. 2018; H. Zhang et al. 2025). Yet these properties are essential for understanding the dark matter halos of LABs, including their masses and occupation fractions, as shown for LAEs (e.g., S. Hong et al. 2019; H. Umeda et al. 2025; D. Herrera et al. 2025). Analyzing these properties across all known LABs has been challenging because of inconsistencies in selection techniques and surface brightness. To robustly characterize LAB statistics, a larger sample from a uniform, well-defined survey is essential.

The One-hundred-deg 2 DECam Imaging in Narrowbands (ODIN) survey, a NSF Optical-Infrared Laboratory (NOIRLab) large survey program, is currently the most extensive survey in both area and volume using three narrowband filters corresponding to the three cosmic slices ($z \sim 2.4, 3.1$ and 4.5). Thus, ODIN overcomes past limitations and provides an opportunity to explore the nature of LABs within the context of large-scale structure, discovering more than 65,000 LAEs, 800 LABs, and about 42 Coma-like clusters over three redshifts (K.-S. Lee et al. 2024).

The extensive coverage of the ODIN survey ($\sim 100 \text{ deg}^2$) necessitates efficient methods for searching for rare objects like $\text{Ly}\alpha$ blobs. In this paper, we employ a hybrid approach to identify $\text{Ly}\alpha$ blobs that addresses the challenge of managing numerous spurious detections while simultaneously pushing the detection threshold to include fainter surface brightness objects.

This paper is organized as follows. In Section 2, we review our ODIN data and describe the Gemini/GMOS observations used for spectroscopic confirmation. In Section 3, we present our two LAB selection methods that are applied to all ODIN data. In Section 4, we report the ODIN LAB samples and their spectroscopic confirmation. We present statistical analyses for the LABs, including the luminosity function and number density evolution. Throughout the paper, we assume a flat Λ CDM cosmology, with $\Omega_M = 0.3$, $\Omega_\Lambda = 0.7$, and $H_0 = 70 \text{ km s}^{-1} \text{ Mpc}^{-1}$.

2. DATA AND OBSERVATION

In this work, we use ODIN’s *N501* narrowband data obtained with the Dark Energy Camera (DECam; B. Flaugher et al. 2015), along with *g* and *r* broadband images from the Hyper Suprime-Cam Subaru Strategic Program (HSC SSP) second public data release (H. Aihara et al. 2019). The narrowband image covers $\sim 12 \text{ deg}^2$ of the extended COSMOS field with a seeing of $0''.9$ on a pixel scale of $0''.27$. The image has a nearly uniform 5σ depth of 25.6 mag in the central 10 deg^2 (V. Ramakrishnan et al. 2023). The narrowband filter has a central wavelength of $\lambda_c = 5014 \text{ \AA}$ and bandwidth of $\Delta\lambda = 76 \text{ \AA}$, designed to be sensitive to redshifted $\text{Ly}\alpha$ emission at $z \sim 3.1$ ($3.09 < z < 3.15$, corresponding to 57 cMpc). We refer readers to K.-S. Lee et al. (2024) for an overview of the ODIN program (e.g., narrowband filter specifications, survey strategy, field definitions, and data products), and V. Ramakrishnan et al. (2023) and N. M. Firestone et al. (2024) for details on the dataset used for LAB and LAE selection at $z \sim 3.1$.

Although the background subtraction procedure is described in K.-S. Lee et al. (2024), we elaborate on it here because of its importance for the detection of low-surface-brightness objects. The large scale background across the field of view is found by fitting a template for a camera reflection pattern and sky gradients by a surface fit. Smaller scale variations within a CCD are determined by detecting and masking sources and measuring the background in blocks of 256×256 pixels ($70 \times 70 \text{ arcsec}$). The blocks are linearly interpolated to every pixel. The chosen block size is large enough to sample the surrounding background of each LAB while avoiding over-subtraction at the blob position and preserving its detection.

We report spectroscopic observations conducted to confirm the LABs. We observed six LAB candidates using Gemini/GMOS (I. M. Hook et al. 2004) in long-slit mode during the 2021A semester as a Fast

Turnaround (FT) program, and in Multi-Object Spectroscopy (MOS) mode during the 2021B, 2023A and 2025A semesters. The primary objective of these programs is to confirm the presence of $\text{Ly}\alpha$ emission lines from ODIN LAB candidates by identifying characteristic $\text{Ly}\alpha$ profiles such as double-peaked or asymmetric profile shapes. We used the B600 grating to obtain moderate sensitivity over a wide spectral coverage (between 4500 \AA and 6800 \AA) including $\text{Ly}\alpha$, C IV and He II at $z \sim 3.1$.

The FT long-slit program targeted ODIN-COSMOS-z3p1-LAB014, the first LAB discovered through our visual inspection. However, the peak of $\text{Ly}\alpha$ emission coincided with a bad column, which enabled redshift confirmation of the LAB but prevented any analysis of the line profile. The MOS mode programs employed five masks: two targeted bright LAB samples, and three focused on LAB candidates in one of the ODIN protoclusters (COSMOS-z3.1-C; V. Ramakrishnan et al. 2023). Each MOS mask includes at least one LAB and 4 – 8 LAE candidates. Fifteen out of 24 LAEs were confirmed through narrow $\text{Ly}\alpha$ profiles and no emission lines were detected in the spectra of the remaining sources that are mostly fainter. Details of the LAE and proto-cluster confirmation are described in V. Ramakrishnan et al. (2025a). Table 1 summarizes our targets, slit widths, spectral resolution, exposure times, and the number of LAEs per mask.

We reduced the data using the Gemini IRAF package and successfully confirmed the $\text{Ly}\alpha$ emission from all the targeted LAB candidates. We report the spectroscopic confirmation in Section 4.2.

3. SELECTION OF $\text{Ly}\alpha$ BLOB CANDIDATES

The precise definition of LAB varies greatly depending on the depth of the data and the selection strategy. In their pioneering work, Y. Matsuda et al. (2004) identifies $\text{Ly}\alpha$ blobs based on their size being larger than point sources in $\text{Ly}\alpha$ images, regardless of the presence of embedded compact LAEs. Thus, due to the combination of this selection method and the depth provided by Subaru telescope, their sample includes LABs with exceptionally diffuse $\text{Ly}\alpha$ emission. Alternatively, Y. Yang et al. (2009, 2010), T. Bădescu et al. (2017), T. Shibuya et al. (2018), H. Zhang et al. (2020) and M. Li et al. (2024) define $\text{Ly}\alpha$ blobs as LAEs with $\text{Ly}\alpha$ sizes larger than those of point sources at given $\text{Ly}\alpha$ luminosities. Similarly, T. Saito et al. (2006) and M. Ouchi et al. (2009) identify $\text{Ly}\alpha$ blobs as sources with sizes in narrow- or intermediate-band images larger than their point spread functions (PSF).

We adopt two complementary methods for selecting $\text{Ly}\alpha$ blobs using the ODIN *N501* dataset. The first is a traditional approach based on cross-matching extended $\text{Ly}\alpha$ sources with LAEs, as demonstrated in previous studies (Y. Yang et al. 2009, 2010; T. Shibuya et al. 2018). To extend our search to diffuse LABs without

Table 1. Summary of Gemini/GMOS observation

LAB ID	Slit width ["]	R^1	T_{exp} [s]	N(LAEs) ²	Note
ODIN-COSMOS-z3p1-LAB004	1.0	844	7000	8	MOS mode; protocluster ³
ODIN-COSMOS-z3p1-LAB012	1.5	562	6000	4	MOS mode
ODIN-COSMOS-z3p1-LAB014	1.5	562	6600	...	Longslit mode; Ly α on the bad column
ODIN-COSMOS-z3p1-LAB018	1.5	562	5100	4	MOS mode
ODIN-COSMOS-z3p1-LAB031	2.0	422	7200	8	MOS mode; protocluster ³
ODIN-COSMOS-z3p1-LAB050	2.0	422	7200	8	MOS mode; protocluster ³

NOTE—Spectral redshifts of LABs are included in Table B1.

¹ Spectral resolution.

² Number of LAEs in the same MOS mask with each ODIN LAB.

³ COSMOS-z3.1-C in COSMOS field from V. Ramakrishnan et al. (2023) and V. Ramakrishnan et al. (2025a).

identifiable LAE counterparts such as those found in the SSA22 field (C. C. Steidel et al. 2000; Y. Matsuda et al. 2004), we develop a new selection technique that does not rely on associated LAEs. This method utilizes forced photometry with *Tractor* (D. Lang et al. 2016a) to identify spatially extended Ly α emission in the absence of compact sources (i.e., galaxies). In the following sections, we describe both the traditional and new LAB selection strategies. Throughout this paper, we refer to the traditional method as the “extended-LAE” method and to the new *Tractor*-based method as the “extended-beyond-continuum” method.

3.1. Extended-LAE Method

We select LABs candidates in two steps, following the approach outlined in Y. Yang et al. (2010): (1) identifying bright cores of LABs (i.e., LAEs), and (2) detecting extended Ly α emission around these galaxies in the continuum-subtracted Ly α images.

We first construct an LAE catalog to cross-match with extended Ly α emission using 2'' diameter aperture, comparable to the seeing of the image, photometry from *SExtractor* (E. Bertin & S. Arnouts 1996). We adopt following criteria for LAE selection as Y. Yang et al. (2010) and T. Bădescu et al. (2017): (1) $N501 < 25.6$, (2) $gr - N501 > 0.8$, corresponding to the rest-frame equivalent width cut, $EW_{\text{rest}} > 20 \text{ \AA}$, and (3) $gr - N501 > 3\sigma_{gr-N501}$, where the $\sigma_{gr-N501}$ is uncertainty of the color ($gr - N501$). The gr represents the continuum only magnitude corresponding to the continuum only flux density ($f_{\text{cont}}^{\text{NB}}$) in Equation 1,

$$\begin{aligned}
 f_{\text{cont}}^{B1} &= \frac{F_{B1} - \epsilon_{B1}F_{\text{NB}}}{\Delta\lambda_{B1} - \Delta\lambda_{\text{NB}}}; \\
 f_{\text{cont}}^{B2} &= \frac{F_{B2} - \epsilon_{B2}F_{\text{NB}}}{\Delta\lambda_{B2} - \Delta\lambda_{\text{NB}}}; \\
 f_{\text{cont}}^{\text{NB}} &= \frac{(\lambda_{B2} - \lambda_{\text{NB}})f_{\text{cont}}^{B1} + (\lambda_{\text{NB}} - \lambda_{B1})f_{\text{cont}}^{B2}}{\lambda_{B2} - \lambda_{B1}}; \\
 F_{\text{line}} &= F_{\text{NB}} - f_{\text{cont}}^{\text{NB}} \Delta\lambda_{\text{NB}}.
 \end{aligned} \tag{1}$$

In the Equation, $\Delta\lambda$ and λ denote the FWHM and the central wavelengths of the filters, respectively. We define the observed flux (F) as the product of $\Delta\lambda$ and flux density (f) to calculate continuum-only flux and line-only map. The $f_{\text{cont}}^{\text{NB}}$ is estimated through linear interpolation between the two broadband fluxes. Here, $B1$ and $B2$ correspond to broadband filters whose central wavelengths are shorter and longer than those of narrowband filters, respectively. For $N501$, $B1$ and $B2$ correspond to the g and r bands. To correct for the differences in central wavelength between the narrow- and broadband filters, as well as the wavelength-dependent transmission, we adopt correction factors ϵ . These are defined as the ratio of the broadband mean throughput within the narrowband FWHM to that within the broadband FWHM. We adopt $\epsilon_g = 1.13$ and $\epsilon_r = 0$. Although this LAE selection method is cruder than the improved hybrid-weighted method (N. M. Firestone et al. 2024), we employ it to ensure a comparable EW in both the Ly α image and the LAEs, consistent with previous works (Y. Yang et al. 2009, 2010; T. Bădescu et al. 2017).

We create a Ly α image by subtracting the continuum-only flux image from the narrow-band image as described in Equation 1. Prior to continuum subtraction, the broadband images are smoothed using Gaussian kernels to match the seeing conditions of the narrowband image.

From the Ly α image, we search for extended Ly α emission as follows: after applying a 7-pixel 2D Gaussian filter with an FWHM of 3 pixels ($\sim 0.8''$), we identify all sources with an isophotal area (A_{ISO}), the area of pixels with $\text{SB} > 1.5\sigma_{\text{SB}_1}$, exceeding $\sim 3 \text{ arcsec}^2$ ($\text{DETECT_MINAREA} = 42 \text{ pixels}$) above a surface brightness threshold of $3.3 \times 10^{-18} \text{ erg s}^{-1} \text{ cm}^{-2} \text{ arcsec}^{-2}$. This SB threshold is selected based on tests using visually identified ODIN LABs. It corresponds to $1.5\sigma_{\text{SB}_1}$, where σ_{SB_1} is the surface brightness limit *per* 1 arcsec^2 aperture ($\sigma_{\text{SB}_1} = 2.2 \times 10^{-18} \text{ erg s}^{-1} \text{ cm}^{-2} \text{ arcsec}^{-2}$). We test the radial variation of surface brightness depth fol-

lowing G. Nagaraj et al. (2025). The depth remains nearly constant within $\pm 5\%$ over 1.5° radius, and varies within $\pm 10\%$ across 90% of the survey area. Therefore, we adopt a constant surface brightness depth and detection threshold, even though the depth becomes shallower toward the edges of the survey area.

The $\text{Ly}\alpha$ image contains numerous artifacts originating from both the narrow- and broadband images, including detector artifacts, internal reflections, and background over-subtraction near bright stars, and galactic cirrus. To mitigate these artifacts, which can mimic diffuse emission in the $\text{Ly}\alpha$ map, we apply a masking procedure to exclude these large and bright artifacts. We first run SExtractor on the g and r band image with $\text{DETECT_THRESH} = 3\sigma_{\text{pix}}$, where the σ_{pix} is a pixel-wise root-mean-square (RMS), and with $\text{DETECT_MINAREA} = 10,000$ pixels ($\sim 700 \text{ arcsec}^2$). The resulting segmentation maps from each band are then combined to create a mask for bright and extended sources.

To account for over-subtracted background regions in broadbands that can mimic $\text{Ly}\alpha$ sources, we run SExtractor on the inverted g and r band images with the same DETECT_MINAREA as above. In this case, we calculate DETECT_THRESH for the negative broadband images using Equation 1 by fixing the F_{line} as $\text{Ly}\alpha$ detection threshold and assuming that only one broadband (e.g., g) contains negative flux while the other has zero flux. This allows us to derive a detection threshold in the negative broadband image that corresponds to the $\text{Ly}\alpha$ detection level of $1.5\sigma_{\text{SB}_1}$. We repeat this for the other broadband image and all resulting masks are combined and applied during the selection process. This eliminates spurious sources and ensure reliable identification of diffuse $\text{Ly}\alpha$ emission.

Even after applying the mask, many artifacts persist because the masking procedure was optimized for clearly identifiable artifacts with large sizes and high detection thresholds. In previous studies with smaller survey areas, such features could be manually rejected through visual inspection. However, this approach is not feasible for the $\sim 100 \text{ deg}^2$ area covered by ODIN. Cross-matching the identified extended sources with compact LAEs solves this problem, as it provides an effective way to eliminate artifacts. A caveat, however, is that this method may miss $\text{Ly}\alpha$ blobs without LAE counterparts, particularly those that are diffuse and have low surface brightness. The next section describes our approach to recovering these diffuse sources.

Among the LAB candidates with LAE counterparts, bright point-like sources can appear as extended $\text{Ly}\alpha$ emitters, as their apparent sizes increase above certain surface brightness thresholds. To ensure that we distinguish true extended sources from bright point sources, we compare the size-luminosity distribution of LAB candidates with that of simulated point sources following Y. Yang et al. (2010). To establish the size-luminosity relation for point sources, we inject approximately 10,000

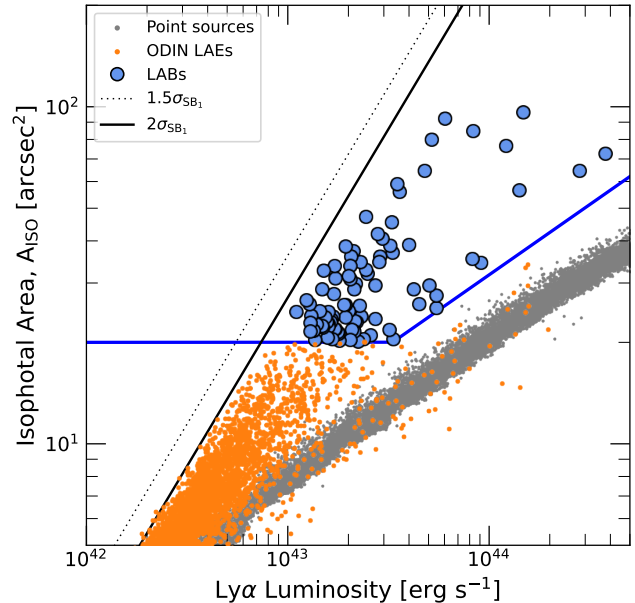


Figure 1. Size-luminosity relation for LAB candidates selected using the extended-LAE selection method. Blue circles represent the LAB candidates. The ODIN LAE sample (orange dots; N. M. Firestone et al. 2024) shows two sequences. One extends to LABs implying that they could be LAH candidates, while the other follows the simulated point sources, indicating that our LAB candidates are distinct from bright and compact point sources. Black dotted and solid lines represent $1.5\sigma_{\text{SB}_1}$ and $2\sigma_{\text{SB}_1}$, respectively, where σ_{SB_1} represents the detection threshold per 1 arcsec^2 . The blue solid lines outline the LAB selection criteria: size over 20 arcsec^2 and 3σ above the size-luminosity relation defined by the simulated point sources.

simulated point sources into empty regions of the $\text{Ly}\alpha$ image. These simulated sources span luminosities from 10^{42} to $10^{45} \text{ erg s}^{-1}$ and are placed to avoid masked areas and existing sources. We measure their sizes and luminosities using the same photometry parameters applied to the LAB candidates.

Figure 1 shows the size-luminosity distribution of the cross-matched LAB candidates, ODIN LAEs and simulated point sources. We isolate 89 LAB candidates (blue circles) with isophotal areas larger than 20 arcsec^2 that lie more than 3σ above the size-luminosity relation defined by the simulated point sources, where σ is the RMS scatter of the simulated point-sources. The independently identified ODIN LAEs (orange dots; N. M. Firestone et al. 2024) shows two sequences. One extends to the LAB size-luminosity relation indicating that these sources could be LAH candidates (M. Ouchi et al. 2020), while the other follows the simulated point sources (grey dots), confirming the reliability of our point source simulation. Some ODIN LAEs are not selected as LABs even though they satisfy the selection criteria. We note

that most of these are identified as LABs using the alternative LAB selection method (Section 3.3).

In Appendix A, we further test whether LAB candidates near the size-luminosity relation of point sources truly exhibit more extended Ly α emission than LAEs with similar Ly α luminosities. We compare the surface brightness profiles of LAB candidates located just above the point source relation with those of LAEs lying within the relation. The LAB candidates show extended surface brightness profiles than LAEs, lending support to the validity of our LAB selection method.

3.2. A New Selection Technique for Diffuse LABs: extended-beyond-continuum Method

While the extended-LAE method effectively identifies a wide range of Ly α blobs, our extensive visual inspection of the ODIN data revealed diffuse and extended Ly α emission (Figure 2) that were not recovered by the selection method described in Section 3.1. These diffuse sources resemble SSA22-LAB18 (Y. Matsuda et al. 2004), which shows low surface brightness without any compact LAE counterparts. When attempting to identify these sources and construct a complete LAB sample, it is necessary to adopt a relatively aggressive detection threshold for both LAEs and LABs. However, this inevitably increases the number of spurious detections, thereby requiring extensive visual inspection due to various artifacts arising from the construction of the continuum-subtracted image (e.g., negative backgrounds from broadband images) over a large survey area. To mitigate this issue and enable source detection without excessive manual inspection, we introduce a new LAB selection method.

The key feature of the new pipeline is the subtraction of all galaxies detected in the broadband image from the narrowband image, enabling direct detection of the remaining extended emission. This approach is conceptually similar to the wavelet decomposition technique (M. K. M. Prescott et al. 2012a), but we extend it by incorporating multi-band information. To efficiently and accurately remove known galaxies from the narrowband image, we adopt a forced-photometry tool, *Tractor*. This tool includes modules for optimizing galaxy shapes and brightness, constructing model images, and performing forced photometry across multiple bands (D. Lang et al. 2016a,b; A. Dey et al. 2019). Using *Tractor*, we extract galaxy model parameters from a broadband image and subtract the corresponding galaxy models from the narrowband image. By using this NB residual image—which is largely free from artifacts arising from broadband subtraction—as the detection image, we can minimize the number of spurious detections, as described below. In the following, we describe the workflow of this *Tractor*-based LAB selection pipeline in detail.

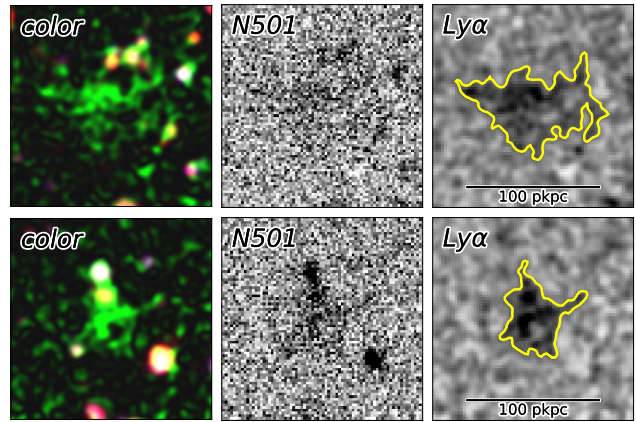


Figure 2. Postage stamp (20×20 arcsec 2) images for examples of diffuse and extended Ly α halos identified by our visual inspection. These objects are not selected as LAB in extended-LAE method, requiring additional LAB selection is necessary for assembling a complete LAB samples. **Left:** Color image constructed with *N501*, *g*, and *r* bands. Green shows the diffuse and extended signal in the *N501* image. **Middle:** High contrast *N501* image revealing the diffuse and extended source. **Right:** Filtered Ly α image. Yellow contours ($1.5\sigma_{\text{SB1}} = 3.3 \times 10^{-18}$ erg s $^{-1}$ cm $^{-2}$ arcsec $^{-2}$) highlighting the diffuse and extended Ly α emission.

(1) *Broadband source detection*—Because *Tractor* requires source positions and initial shape parameters, we begin by detecting sources in the HSC SSP *g*-band image using *SExtractor*. Detecting objects near bright sources is particularly challenging, as *SExtractor* tends to overestimate the local background in such regions, reducing sensitivity to nearby faint sources. These undetected objects may persist in both the broadband and narrowband images and can be mistakenly identified as LABs. To mitigate this issue, we adopt a lower detection threshold (DETET.THRESH = 0.9 and DETECT_MINAREA = 4 pixels), which improves completeness while introducing more false detections. However, these false detections are not a critical concern because the *Tractor* will assign them near-zero flux in the narrowband images, effectively excluding them from the final residual image.

(2) *Cutout images*—We cut out sky-subtracted *g*-band and *N501* images into 64×64 pixel sub-tiles. This small tile size reduces computation time by limiting the number of galaxies modeled in each sub-tile. However, when a galaxy falls near the edge of a sub-tile, the *Tractor* modeling procedure may fail. To avoid this issue, we introduce overlapping sub-tiles with a half-tile offset in both the X and Y directions (Figure 3). This overlap minimizes galaxy fragmentation at tile boundaries and improves model accuracy.

If the source size is significantly larger than 64 pixels on a side, *Tractor* tends to underestimate its size, often modeling the object as a point source. However, this

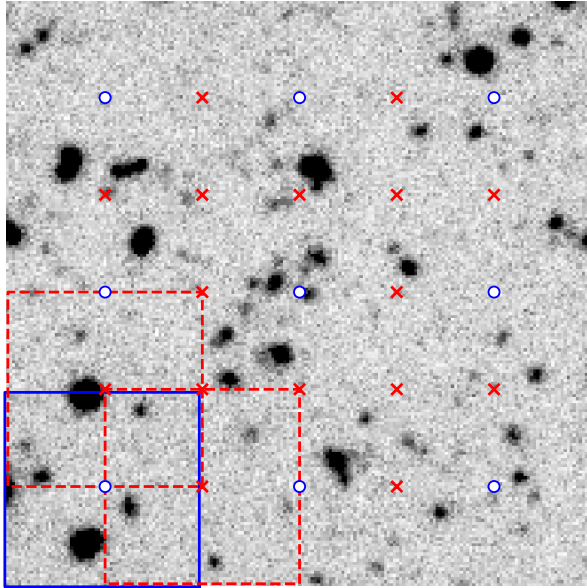


Figure 3. Example 192×192 pixel² ($52'' \times 52''$) HSC SSP g band image that illustrates our tiling strategy. We use 64×64 pixel² sub-tile images to perform model fitting for g -band galaxies. To ensure accurate model fitting and avoid fragmentation near the sub-tile edges, We offset each tile by half a tile-size from its nearest adjoining tile. This pattern is illustrated by the solid blue and red dashed squares, whose centers are defined by the blue circles and red crosses, respectively.

does not critically affect our analysis, as such sources are low-redshift galaxies and will be excluded by the EW_{rest} criterion applied in the final step of this method.

(3) *Extract galaxy shape*—Galaxy shapes are modeled from the broadband (g) image using *Tractor*. To optimize galaxy fits, *Tractor* convolves each source model with the image PSF (constructed with *PSFEx*) and determines the best-fit model and integrated flux density by χ^2 minimization. We adopt six different *Tractor* source models: *PointSource*, *GaussianGalaxy*, *ExpGalaxy*, *DevGalaxy*, *SersicGalaxy*, and *FixedCompositeGalaxy* corresponding to a point source, a gaussian profile, an exponential profile, a de Vaucouleurs profile (G. de Vaucouleurs 1948), a Sersic profile (J. L. Sérsic 1963) and the combination of *ExpGalaxy* and *DevGalaxy* models. They are defined by position, brightness and elliptical shape. The elliptical shape is parameterized by *EllipseESoft*, the sigmoid-softened ellipticities provided by *Tractor*. Initial input parameters for the model fitting are taken from the *SExtractor* output (e.g., *FLUX_AUTO*, *A_IMAGE*, *B_IMAGE*, and *THETA_IMAGE*). To avoid over-estimation of galaxy sizes, we impose a size limit of $r_e < 10''$ (50 pixels) based on repeated tests. For the same reason noted

above, this upper limit does not affect results because it will be removed in subsequent steps. If a galaxy appears in multiple overlapping sub-tiles, we keep only the model from the sub-tile in which the galaxy is closest to the tile center.

(4) *Construct N501 Model and Residual images*—We perform *forced* photometry on the *N501* image using the source models obtained in the step (3). In this step, only the amplitudes of the model components are fitted, while the shapes and positions remain fixed. The philosophy of our technique is to remove all features attributable to galaxies, thereby minimizing stellar components while preserving extended emission from the CGM. *Tractor* generates a best-fit image by convolving the source models with the *N501* PSF. Figure 4 shows an example of a *Tractor* model and the corresponding residual images, in which compact sources have been subtracted, leaving only the extended $\text{Ly}\alpha$ emission. By subtracting the model image (“N501 model”) from the observed *N501* image (“N501”), we obtain a residual map (“N501 residual”) that highlights extended emission without continuum. To avoid missing sources larger than the cutout size, we construct the model image to match the full coverage of the observed *N501* field, and detection is performed on this image in the subsequent step.

(5) *Detection and Measurement*—We convert the residual *N501* map to the residual $\text{Ly}\alpha$ map assuming that the continuum emission has been effectively modeled and removed. We detect LAB candidates from this residual $\text{Ly}\alpha$ map after filtering the image with the same Gaussian kernel and applying the same detection criteria used in the extended-LAE pipeline: a SB threshold of 3.3×10^{-18} erg s⁻¹ cm⁻² arcsec⁻² and a minimum isophotal size of 3 arcsec² (see Section 3.1). We note that this model-subtracted and smoothed $\text{Ly}\alpha$ image is used solely for source detection. For measuring isophotal sizes and fluxes, we use the continuum-subtracted $\text{Ly}\alpha$ -only image from Section 3.1 to ensure fair $\text{Ly}\alpha$ luminosity and size measurements. We employ the *ASSOCIATION* feature of *SExtractor* to link detections from the residual image (from *Tractor*) with their corresponding measurements in the continuum-subtracted image (from extended-LAE method).

Figure 5 illustrates the advantages of using the residual $\text{Ly}\alpha$ image from the extended-beyond-continuum method for selecting diffuse sources. If we use the $\text{Ly}\alpha$ image from the extended-LAE method (i.e., $\text{NB} - gr$) as detection image, the over-subtracted background near the artifact (a reflected stripe in Figure 5) leads to numerous false detections (yellow contours) as *SExtractor* splits them into clumps of various sizes. The residual $\text{Ly}\alpha$ image from *Tractor* avoids this issue by relying solely on the narrowband image and proper modeling of continuum sources. As a result, the extended-beyond-continuum method significantly reduces the number of spurious detections and alleviates the need for extensive

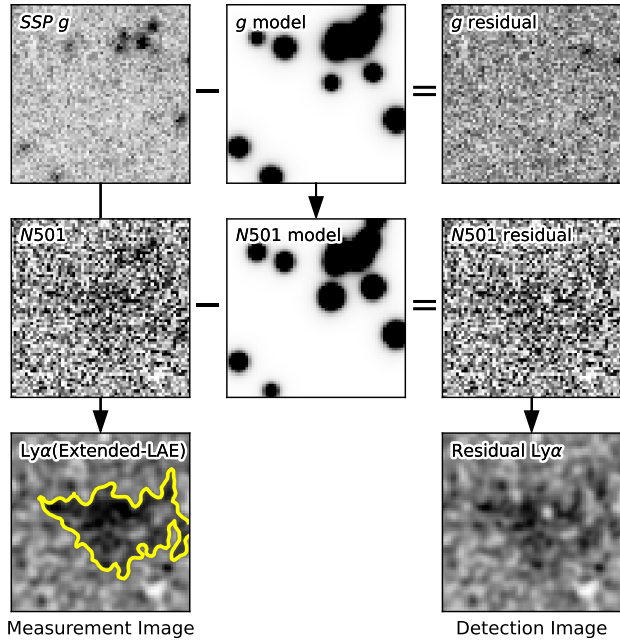


Figure 4. Postage stamp images (64×64 pixel²) demonstrating extended-beyond-continuum method. **Top row:** HSC SSP g -band image (left), the **Tractor** model image of galaxies (center), and the residuals from the fits (right). The **Tractor** models do an excellent job reproducing the continuum emission from the galaxies. **Middle row:** the same set of images for the $N501$ frame. The galaxy models have the exact same shape parameters as for the g -band data. Note the excess $\text{Ly}\alpha$ flux on the residual image. **Bottom row:** The residual $\text{Ly}\alpha$ image which is used for the detection of LABs in the extended-beyond-continuum method (right). The image is constructed by only the residual $N501$ image. The flux and sizes are measured using the $\text{Ly}\alpha$ image from extended-LAE method (left).

visual inspection, which inevitably introduces subjective bias.

(6) *LAB Candidate Selection*—We select LAB candidates using the same criteria described in Section 3.1, with a EW_{rest} cut based on isophotal fluxes: (1) an isophotal area larger than 20 arcsec^2 , (2) a 3σ measurement above that predicted from the point-source size-luminosity relation, and (3) $\text{EW}_{\text{rest}} > 20\text{\AA}$, matching the equivalent width threshold used for LAEs in the extended-LAE pipeline. Figure 6 shows the LAB candidates selected by the extended-beyond-continuum pipeline (red circles) on the size–luminosity diagram.

The new method identifies 95 LABs, including 23 newly discovered LABs. Out of the 89 LABs identified by the extended-LAE method, 72 are also recovered by the extended-beyond-continuum pipeline, demonstrating the consistency and reliability of both LAB selection methods. On the other hand, there are 17 LABs that

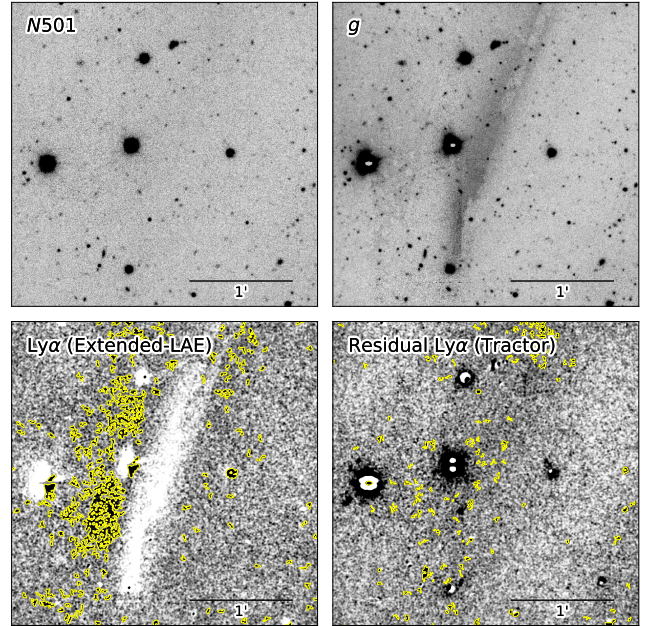


Figure 5. Cutout images ($3' \times 3'$) illustrating the robustness of the **Tractor**-based residual $\text{Ly}\alpha$ detection image. **Top:** $N501$ and g band images. A bright internal reflection (dark stripe) is clearly visible across the g -band image, introducing large-scale artifacts. **Bottom:** $\text{Ly}\alpha$ detection images from the extended-LAE (left) and the extended-beyond-continuum methods, respectively. Yellow contours indicate regions exceeding the detection threshold for $\text{Ly}\alpha$ blob candidates identified by **SExtractor**. In the extended-LAE method (Section 3.1), the artifact is propagated into the $\text{Ly}\alpha$ detection image, and the over-subtracted background near this artifact leads to numerous false detections (yellow contours). In contrast, the residual $\text{Ly}\alpha$ image from **Tractor** is effectively free of this artifact, significantly reducing spurious detections.

are not recovered by the extended-beyond-continuum method because their measured sizes fall below the minimum detection area ($< 3 \text{ arcsec}^2$). This sometimes occurs when forced photometry removes the galaxy component: the bright core of the $\text{Ly}\alpha$ emission in the $N501$ image can be over-subtracted, creating a hole in the NB–continuum image and leaving only a smaller $\text{Ly}\alpha$ halo in the residual image that does not meet the minimum area threshold. Consequently, the LAB catalogs produced by the extended-LAE and the extended-beyond-continuum approaches are complementary, and together they provide a more complete LAB catalog.

3.3. Comparison of the Two Selection Methods

To compare the LAB samples selected by the extended-LAE and extended-beyond-continuum methods, we compute the average surface brightness of each sample. As shown in Figure 7, the extended-beyond-continuum pipeline is effective at identifying LABs with

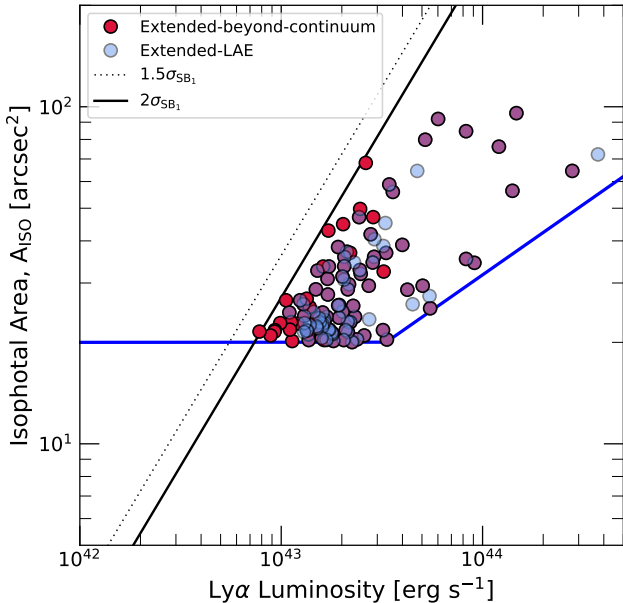


Figure 6. Same as Figure 1, but for both of the selection methods. Blue circles represent LABs identified using the extended-LAE pipeline described in Section 3.1, while red circles denote LAB candidates from the extended-beyond-continuum method. Of the 89 LABs from the extended-LAE method, 72 are also recovered by the extended-beyond-continuum pipeline, indicating the robustness of our LAB selection and the reliability of the sample. LABs identified only by the extended-beyond-continuum method tend to exhibit lower surface brightness and lie closer to the $2\sigma_{\text{SB}_1}$ limit (black solid line), suggesting that the method effectively identifies diffuse LABs missed by traditional methods.

low surface brightness. Notably, out of 112 total LABs, 23 (20%) are uniquely identified by the extended-beyond-continuum pipeline.

The extended-beyond-continuum method is also capable of detecting dual-LAE systems (e.g., Figure 8, LAB024), which are typically missed by the extended-LAE pipeline. In these cases, **SExtractor** deblends the dual-LAE into two separate compact LAEs, artificially reducing the apparent size of the extended $\text{Ly}\alpha$ emission. In contrast, in the extended-beyond-continuum pipeline, the continuum sources (i.e., the primary source peaks) are effectively removed from the detection image by modeling. Therefore the de-blending is not triggered. The extended-beyond-continuum pipeline detects the diffuse, extended $\text{Ly}\alpha$ halo directly, thus preserving the full extent of the emission and enabling the identification of this interesting class of LABs.

In terms of pipeline complexity and required human effort, the visual inspection of low-surface-brightness features is substantially less demanding in the extended-beyond-continuum approach. For example, in the extended-LAE method, the initial size–luminosity cut

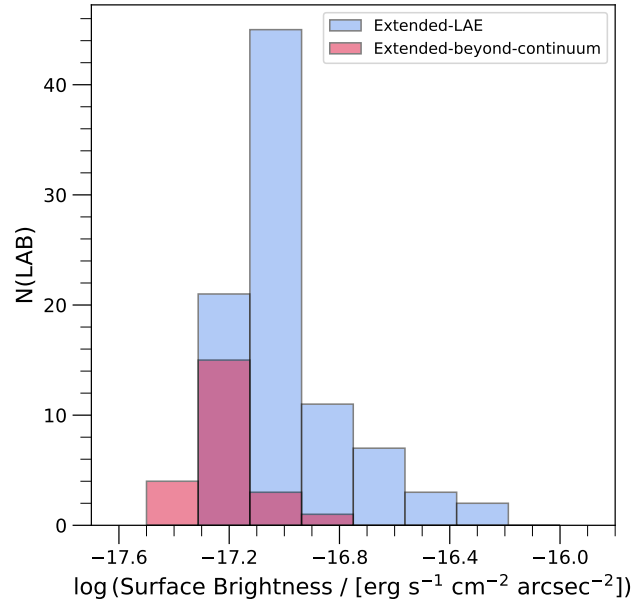


Figure 7. Average surface brightness within the isophotes for the extended-LAE pipeline and the extended-beyond-continuum pipeline. The bin size (0.1875 in a log) is defined following D. W. Hogg (2008). The LABs recovered only with the extended-beyond-continuum pipeline (red) have lower surface brightnesses.

yields $\sim 10,000$ extended *features*, which must then be cross-matched with LAEs to reduce the sample to ~ 280 candidates, followed by visual inspection to obtain the final sample of 89 LABs. In contrast, the extended-beyond-continuum method reduces the initial number of extended features to only ~ 250 , smaller by a factor of ~ 40 compared to the extended-LAE method, thereby greatly simplifying the visual inspection process.

On the other hand, LABs identified by the extended-LAE method have been spectroscopically confirmed over the past two decades (e.g., T. Yamada et al. 2012; Y. Yang et al. 2011, 2014; T. Shibuya et al. 2018; H. Zhang et al. 2020; M. Li et al. 2024), making them a reliable benchmark for validating the performance of the extended-LAE pipeline. However, the method is less sensitive to low surface brightness LABs and tends to miss dual-LAE systems.

To construct a more complete and robust LAB sample while minimizing the need for intensive visual inspection and mitigating artifacts in large survey areas, we adopt both selection methods in parallel.

3.4. Recovery Test and Uncertainties

To evaluate the reliability of detections and quantify uncertainties in the sizes and luminosities of LAB candidates, we conduct a recovery test following the method of Y. Yang et al. (2009). We extract a smoothed $\text{Ly}\alpha$ postage stamp image ($25 \times 25 \text{ arcsec}^2$) for each LAB candidate and inject it into $\sim 4,000$ randomly se-

lected empty sky regions within the Ly α image. The empty sky regions are defined as the survey areas that avoid detected sources and masked regions, based on the **SExtractor** segmentation map and the masks described in Section 3.1. We then perform the same isophotal photometry and apply the LAB selection criteria described in Section 3.1 to the injected sources.

We evaluate how many of the injected mocks are successfully recovered based on the size–luminosity selection criteria (blue line in Figure 6). The recovery fraction (f_{recv}) for each LAB is defined as the ratio of recovered mocks to the total number of injected mocks. To eliminate outliers caused by unmasked faint halos of bright sources or over-subtracted sky regions, we apply a 3σ clipping algorithm to the distribution of recovered luminosities prior to computing f_{recv} . Variations in surface brightness depth across the image lead to fluctuations in the apparent sizes of LABs, which in turn affect their likelihood of being selected as LABs. We adopt the standard deviations of the recovered size and luminosity distributions as the uncertainties associated with each source.

The majority of LABs (99%) are recovered with a recovery fraction $f_{\text{recv}} > 0.5$. A substantial fraction of LABs (71%) exhibit $f_{\text{recv}} > 0.95$. The recovery fractions, along with the uncertainties in size and luminosity, are included in the final Ly α blob catalog (Table B1).

4. RESULTS AND DISCUSSION

4.1. LABs in E-COSMOS at $z \sim 3.1$

We discover a total of 112 Ly α blobs using both the extended-LAE and the extended-beyond-continuum selection methods. This constitutes one of the largest LAB samples to date, covering a wide survey area of $\sim 9 \text{ deg}^2$ with a uniform surface brightness threshold. We expect the LAB sample to grow substantially as the ODIN survey progresses to its goal of $\sim 100 \text{ deg}^2$ coverage across three redshift windows. Figure 8 presents RGB postage stamp images of the LABs, constructed using HSC SSP r , ODIN $N501$, and HSC SSP g bands as the red, green, and blue channels, respectively.

Table B1 lists the key properties of LABs: source ID, coordinates, Ly α luminosity, isophotal areas, end-to-end extents of the Ly α contour, and recovery fractions. Within the catalog, the LAB IDs are assigned in order of decreasing luminosity Ly α , with lower ID numbers corresponding to brighter sources. We also indicate which selection method was used to identify each LAB. We highlight a few notable examples from the LAB sample.

ODIN-COSMOS-z3p1-LAB001 is the most luminous LAB in our sample, exhibiting a narrow, linear feature extending toward the east. To access the robustness of this diffuse linear structure, we perform a bootstrap test by combining subsets of the exposures. We randomly choose five exposures from ten exposures and construct a stacked image. We repeat this 100 times and confirm

that the narrow and elongated Ly α structure persists, indicating that the observed morphology is not an artifact from certain exposure combinations.

ODIN-COSMOS-z3p1-LAB009 appears to be a pair of LAB or an interacting system with $\sim 150 \text{ kpc}$ end-to-end size. Recently, deep VLT/MUSE observations discovered much larger ($\sim 700 \text{ pkpc}$) Ly α nebulae pair at $z \sim 3$. This system consists of a QSO pair and a Ly α filament connecting them (E. Lusso et al. 2019; D. Tornotti et al. 2025). Measurement of systematic redshifts of two components and deep IFU observation could provide insight into the nature of this source. We redefine their positions as the mean coordinate of the two spatial peaks of the Ly α emissions.

ODIN-COSMOS-z3p1-LAB024 consists of the two LAEs that are individually listed in the ODIN-LAE catalog (N. M. Firestone et al. 2024). In the extended-LAE pipeline, the source is deblended into two components by **SExtractor**. In contrast, the extended-beyond-continuum pipeline does not deblend the system, as it removes the compact galaxies and retains only the diffuse, connected Ly α halo. Since no distinct sources remain in the residual image, deblending is not triggered, and the halo is detected as a single extended structure. We classify this type of object as a “dual-LAE” system.

ODIN-COSMOS-z3p1-LAB028 exhibits a tail-like feature extending toward the northeast. Because of a continuum source between the tail and the central emission, it is deblended by the current pipeline and the tail is not included as part of this LAB.

ODIN-COSMOS-z3p1-LAB031 is one of the LABs identified by initial visual inspection and later recovered by the extended-beyond-continuum pipeline. It exhibits a large, diffuse Ly α halo with only a faint optical counterpart visible in the HSC SSP g -band image, indicating the absence of any clearly identifiable powering source. This example highlights the effectiveness of the extended-beyond-continuum pipeline in discovering low-surface-brightness LABs that may be missed by traditional methods.

ODIN-COSMOS-z3p1-LAB084 is associated with a galaxy group exhibiting an extended Ly α halo. Previous Keck/KCWI observations (RO-0959; E. Daddi et al. 2022) yield a systemic redshift of ~ 3.096 , placing it near the blue edge of the $N501$ filter transmission curve (K.-S. Lee et al. 2024). Despite the reduced filter throughput at this redshift, RO-0959 is still robustly selected as a LAB, confirming the reliability of the ODIN LAB sample.

We note that the LAB catalog in the E-COSMOS field at $z = 3.1$ has been updated relative to V. Ramakrishnan et al. (2023), which identified 122 LABs without applying the extended-beyond-continuum method. In the earlier catalog, the sizes of some LABs were slightly overestimated due to imperfect deblending, allowing certain sources to exceed the size selection criterion and

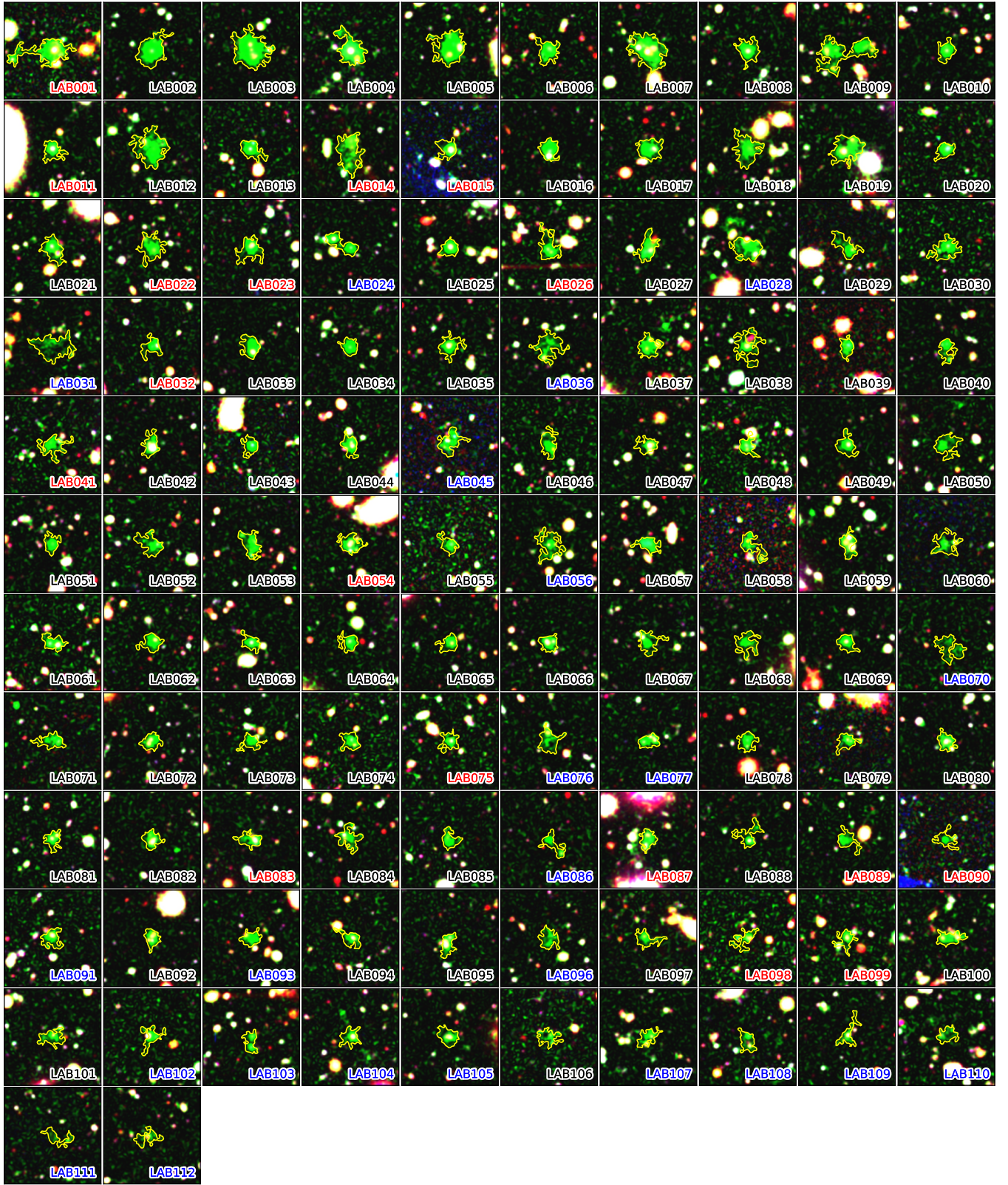


Figure 8. 30×30 arcsec² postage stamp RGB images of 112 LABs. The color represented are composed of Subaru/HSC r (red), ODIN $N501$ (green), and Subaru/HSC g (blue) images. In each case, the yellow contours indicate the surface brightness detection threshold ($1.5\sigma_{\text{SB}_1} = 3.3 \times 10^{-18} \text{erg s}^{-1} \text{cm}^{-2} \text{arcsec}^{-2}$). The LAB IDs are colored red, blue, and black, corresponding to LABs selected only by the extended-LAE method, only by the extended-beyond-continuum method, and by both methods, respectively.

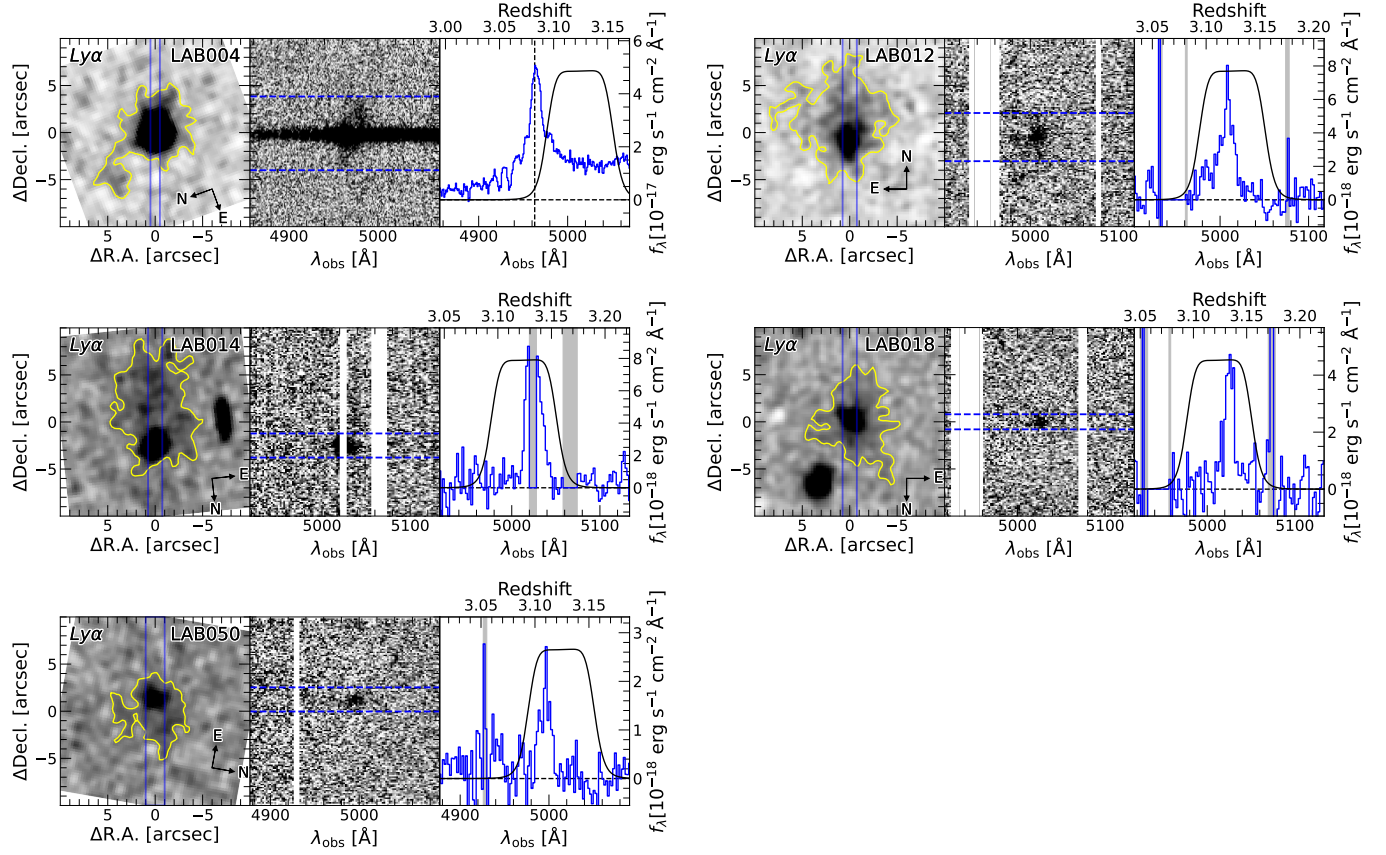


Figure 9. Gemini/GMOS spectra (Section 2) alongside Ly α images. The first column in each panel shows the Ly α image with the GMOS slit position overlaid in blue. The second column is the corresponding 2D spectrum; blue dashed lines indicate the apertures used for extracting the 1D spectrum. The vertical axis corresponds to the spatial direction, aligned with the orientation in the Ly α images. The third column displays the extracted 1D spectrum in the vicinity of Ly α , overlaid with the $N501$ filter transmission curve (in arbitrary units). The Gray-shaded regions indicate areas affected by poor sky subtraction or bad columns. For LAB004, The black dashed vertical line indicates the redshift measured from the He II $\lambda 1640$ emission line. The detection of spatially extended Ly α emission even at the $N501$ filter bandpass edge supports the reliability of our LAB selection.

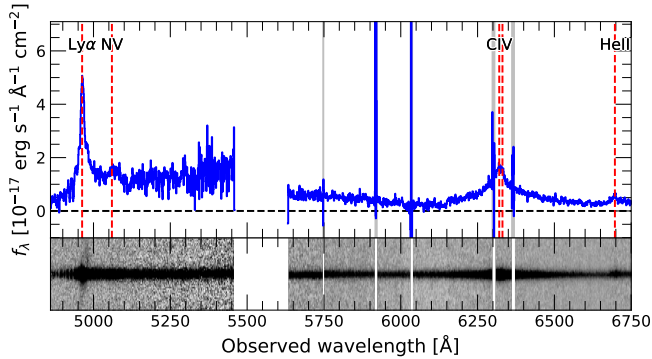


Figure 10. Gemini/GMOS 1D and 2D spectrum for LAB004 and a central QSO. The gray-shaded regions indicate areas affected by poor sky subtraction or bad columns. A large gap at $\lambda \sim 5550$ Å is because of the bad amplifier. Red dashed lines indicate observed emission lines. The broad hard ionization lines (N V and C IV) implies that the QSO is the powering source of LAB004.

thus be classified as LABs, inflating the sample size. Nevertheless, approximately 70% of the LABs are common to both catalogs. Importantly, the scientific results presented in V. Ramakrishnan et al. (2023) and in this work remain unchanged regardless of which catalog is used.

4.2. Spectroscopic Confirmation

Five out of six LABs are spectroscopically confirmed through our Gemini/GMOS program. We successfully detect $\text{Ly}\alpha$ emission for the five LABs in both the 1D and 2D spectra. $\text{Ly}\alpha$ emission is not detected from LAB031, which has one of the lowest surface brightnesses, because the Gemini/GMOS observations are approximately a factor of two shallower than the ODIN data. Figure 9 presents the $\text{Ly}\alpha$ spectra for these sources. Among them, two (and possibly three) LABs exhibit spatially extended $\text{Ly}\alpha$ emission in the 2D spectra, consistent with their classification as extended halos.

ODIN-COSMOS-z3p1-LAB004—This object shows not only a clear continuum but also spatially extended $\text{Ly}\alpha$ emission. Broad rest-frame UV emission lines (N V and C IV) and relatively narrow He II emission ($\text{FWHM} = 549 \pm 32 \text{ km s}^{-1}$) are also detected (Figure 10). While the peak of the $\text{Ly}\alpha$ emission lies near the edge of the N501 filter bandpass, the spatially extended component extends to wavelengths where the filter transmission is $\sim 50\%$ (~ 4990 Å), ensuring that a significant portion of the $\text{Ly}\alpha$ emission is still captured by the narrowband imaging.

We estimate the spectroscopic redshift to be $z = 3.0825 \pm 0.0002$ based on the He II emission line. Interestingly, the peak wavelength of the $\text{Ly}\alpha$ emission closely matches the systemic redshift derived from He II, sug-

gesting either direct photoionization by a central AGN (A. Dey et al. 2005; Y. Yang et al. 2014; V. Langen et al. 2023), or the presence of clumpy neutral hydrogen clouds within the CGM that allows for efficient $\text{Ly}\alpha$ escape without significant resonant scattering (M. Gronke 2017; S.-J. Chang et al. 2023).

ODIN-COSMOS-z3p1-LAB012—We confirm spatially extended $\text{Ly}\alpha$ emission over $\sim 5''$ in the GMOS 2D spectrum. This extended emission coincides with the brightest region of the $\text{Ly}\alpha$ blob.

ODIN-COSMOS-z3p1-LAB014—The peak of $\text{Ly}\alpha$ emission coincided with a bad column, allowing us to confirm the redshift of the LAB but preventing analysis of the line profile. Spatially extended $\text{Ly}\alpha$ emission is marginally detected on the red side of the bad column.

ODIN-COSMOS-z3p1-LAB018 and LAB050—Figure 9 shows a compact and narrow $\text{Ly}\alpha$ emission in both the 2D and 1D spectra. The detection of only a single emission line within the $3600\text{Å} - 6730\text{Å}$ spectral range strongly suggests that the feature is not from a lower-redshift source. Lower redshift features such as C IV, He II, [O II], and [O III] would typically be accompanied by additional bright emission lines in the GMOS spectra. The absence of spatially extended diffuse $\text{Ly}\alpha$ emission may be due to the relatively short exposure time and/or missing the low surface brightness part.

To further test the reliability of our LAB candidates, we cross-match them with known spectroscopic redshifts from the literature. We use datasets from SDSS-DR14Q (I. Pâris et al. 2014), PRIMUS (R. J. Cool et al. 2013), zCOSMOS (S. J. Lilly et al. 2009), Subaru/FMOS survey (J. D. Silverman et al. 2015), 3D-HST grism survey (I. G. Momcheva et al. 2016), MOSDEF survey (M. Kriek et al. 2007), DEIMOS 10k survey (G. Hasinger et al. 2018) and other literatures. In addition, we visually inspect DESI DR1 spectra (DESI Collaboration et al. 2025) of 45 DESI targets that coincide with the positions of LABs. We confirm $\text{Ly}\alpha$ emission in 40 LABs regardless of DESI redshift. HETDEX successfully confirm $\text{Ly}\alpha$ emission from one LAB (G. J. Hill et al. 2021 and Mentuch Cooper et al. in preparation). We confirm the redshift of six LAB from Keck/DEIMOS observation (V. Ramakrishnan et al. 2025a). In summary, we find that 52 LABs (out of a total of 112) with known spectroscopic redshifts are consistent with $z \sim 3.1$ without lower-redshift interlopers (Table B1). This constitutes one of the largest spectroscopically confirmed LAB samples to date.

4.3. Environmental Effects on Number density and Luminosity.

The number density and luminosity function (LF) of LABs remain poorly constrained due to their rarity and strong field-to-field variation (e.g., Y. Yang et al.

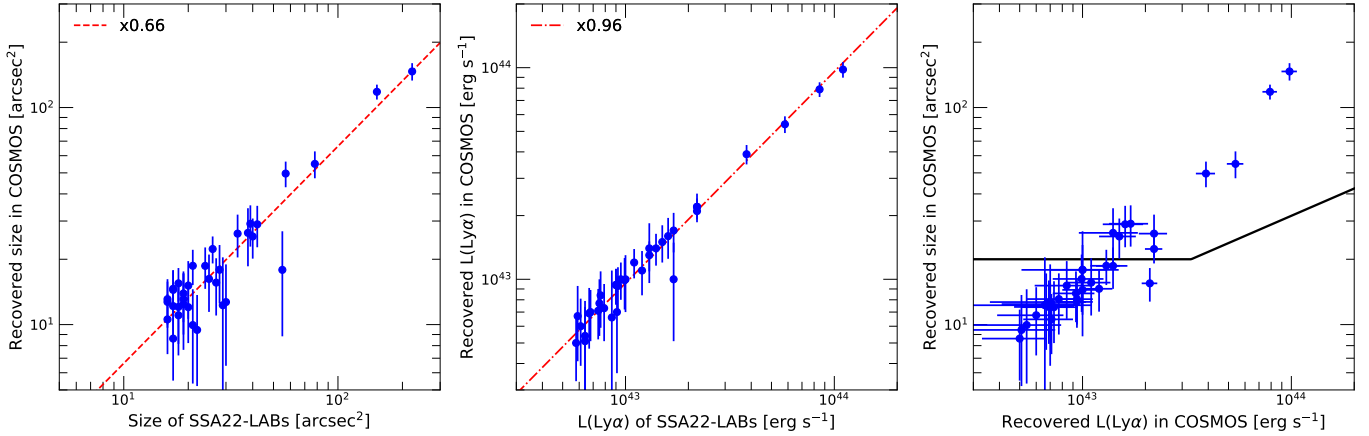


Figure 11. Recovery test results for SSA22 LABs. **Left:** Recovered isophotal size vs. original size. **Middle:** Recovered luminosity vs. original luminosity. **Right:** The recovered size–luminosity relation for the SSA22 LABs overlaid with ODIN LAB selection criteria. Because of ODIN’s shallower surface brightness depth, the sizes and luminosities of the SSA22 LABs would be measured as smaller than their original values by factors of ~ 0.66 and ~ 0.96 , respectively. Ten of the 35 SSA22 LABs would be recovered as LABs under the ODIN selection criteria in the size–luminosity diagram (black solid line). For a fair comparison, we adopt the number density derived from this recovery test for the SSA22 LABs.

2010). Furthermore, different selection criteria and survey depths across studies make statistical analyses particularly challenging. With one of the largest LAB samples to date from the ODIN survey, we investigate the LAB luminosity function and its dependence on environment. ODIN enables a significant breakthrough, offering a large survey area with a uniform surface brightness threshold and environment information, all of which are crucial for obtaining reliable statistical analysis.

A detailed analysis of the redshift evolution of LABs and field-to-field variation across the disjoint ODIN survey fields will be presented in a forthcoming paper (B. Moon in preparation). In this work, we present initial results on the number density and luminosity functions (LFs) of LABs in the E-COSMOS field, which hosts two massive proto-clusters (V. Ramakrishnan et al. 2023, 2024, 2025b).

We measure the number density of LABs across the entire E-COSMOS survey area (9 deg^2 ; $6.5 \times 10^6 \text{ cMpc}^3$ assuming the FWHM of the $N501$ filter as the line-of-sight thickness), as well as within the overdense regions (i.e., proto-clusters) separately. For the entire survey area, the number density of LABs at $z \sim 3.1$ is $n = 1.7 \pm 0.2 \times 10^{-5} \text{ cMpc}^3$, with the uncertainty coming from the Poisson shot noise of the LAB number counts. To enable direct comparison with previous works, we also compute the LAB number density within a survey area equivalent to that used by Y. Matsuda et al. (2004): a $31' \times 23'$ FOV (0.2 deg^2), typical of pre-HSC and pre-DECam surveys. Moreover, the similar survey redshifts allow us a direct comparison of LAB number densities between our sample and that of the SSA22 proto-cluster field, one of the most well-studied overdense environments. Within the sampling box that encompasses the most overdense regions (Complexes A

and C; V. Ramakrishnan et al. 2023) with a local 2D surface overdensity of $\delta_\Sigma \sim 5.5$ comparable to the SSA22 proto-cluster (C. C. Steidel et al. 2000; Y. Matsuda et al. 2011), we identify 11 and 8 LABs in each complex, respectively. This yields a significantly elevated number density of $6.5 \pm 1.5 \times 10^{-5} \text{ cMpc}^{-3}$ on average, a factor of ~ 4 higher than that of the entire E-COSMOS LAB sample.

For a direct comparison with the SSA22 sample, which has a deeper detection threshold of $2.2 \times 10^{-18} \text{ ergs}^{-1} \text{ cm}^{-2} \text{ arcsec}^{-2}$ than the ODIN survey, we test how many SSA22 LAB would be recovered as LABs under the shallower depth of the ODIN survey, using the same methodology described in Section 3.4. For each SSA22 LAB, we inject its image into 4,000 empty sky regions in the ODIN $\text{Ly}\alpha$ image and measure the median recovered isophotal sizes and luminosities at our detection threshold. The uncertainties are estimated as the standard deviations of these measurements. Figure 11 shows that the recovered SSA22 LABs, if observed by ODIN, would have isophotal sizes that are, on average, $\sim 66\%$ smaller than the original measurements by Y. Matsuda et al. (2004), due to the shallower depth. Out of the 35 SSA22 LABs, ten would meet the LAB selection criteria in the ODIN survey, resulting in a number density of $n = 7.7 \pm 2.4 \times 10^{-5} \text{ cMpc}^{-3}$. This recovered number density is consistent with that of the ODIN LABs found in proto-cluster regions.

Figure 12 presents the cumulative luminosity function (CLF) of ODIN LABs across the entire E-COSMOS field, the CLF measured in the two proto-cluster complexes, and the CLFs of the SSA22 LABs (Y. Matsuda et al. 2004), located in the SSA22 proto-cluster (both original and recovered). We fit the CLFs with a linear function in logarithmic space, $\log n = A \log L(\text{Ly}\alpha) + B$.

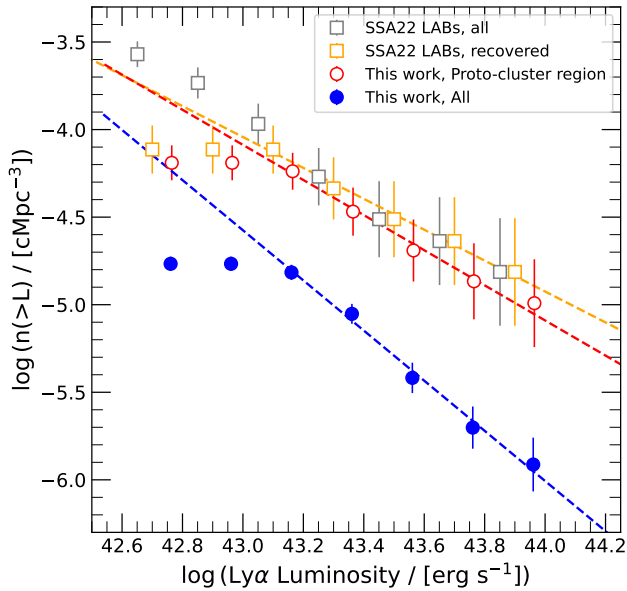


Figure 12. Cumulative luminosity functions (CLFs) of the SSA22 and E-COSMOS LABs. Data points are slightly offset for clarity. Proto-cluster-associated LABs are shown as open symbols, while blue filled circles represent all ODIN LABs across the E-COSMOS field. The dashed lines indicate linear fits to the CLFs of each LAB sample. The flatter slopes and higher amplitudes of the proto-cluster-associated LAB CLFs suggest that the $\text{Ly}\alpha$ luminosities and number densities of LABs are environment-dependent.

The slope of the CLF for the full E-COSMOS LAB sample is -1.4 ± 0.1 , steeper than those of the proto-cluster-associated LABs (-0.9 ± 0.1 and -1.0 ± 0.1 for the recovered SSA22 LABs and for the ODIN LABs in Complex A and C, respectively).

Our initial results with still limited sample size (29 LABs within three proto-clusters) suggest the possibility of environmental effects on number density and luminosity of $\text{Ly}\alpha$ blobs (e.g., Y. Matsuda et al. 2011; T. Bădescu et al. 2017; V. Ramakrishnan et al. 2023). To robustly characterize the luminosity function of LABs as a function of environment, an even larger sample is required. ODIN is poised to deliver such a dataset, with an expected sample of $\sim 1,000$ LABs across multiple fields. This will enable detailed investigations into the environmental dependence of LAB luminosity functions and help disentangle the physical mechanisms that power their extended $\text{Ly}\alpha$ emission.

4.4. Number Density Over Cosmic Time

We compare the number density of the ODIN LAB sample with those from previous surveys across a range of redshifts (Figure 13). For this comparison, we adopt the published values from each survey, taking only surface brightness dimming into account. We do *not* correct for differences in survey depth or selection method. This

plot is intended to illustrate the current status of LAB surveys, not the accurate redshift evolution. We compile narrow- and intermediate-band surveys with survey areas larger than 0.2 deg^2 , comparable to that of Y. Matsuda et al. (2004). We exclude shallow but wide surveys (e.g., D. J. B. Smith & M. J. Jarvis 2007; Y. Yang et al. 2009) that focused on large and bright LABs, as they tend to miss smaller LABs, making it difficult to compare number densities consistently. A detailed analysis of larger sample of ODIN LABs, accounting for survey depth, selection methods, and completeness corrections, will be presented in a forthcoming paper (B. Moon, in preparation).

We note that only the $z = 3.1$ samples (ODIN E-COSMOS and SSA22) are suitable for direct comparison as described in Section 4.3. Therefore, all other number density measurements are treated either as upper limits or shown as their original values, for the reasons outlined below. First, we adopt the non-detections from the low-redshift LAB survey by W. C. Keel et al. (2009) as an upper limit. Second, the samples at $z \sim 2.3\text{--}2.4$ (Y. Yang et al. 2010; M. Li et al. 2024) are also treated as upper limits, since they would suffer from surface brightness dimming and drop out of the selection if placed at $z = 3.1$. This effect would lead to smaller apparent sizes and lower recovery fractions, thereby decreasing the inferred number densities. Note that the number densities reported by M. Li et al. (2024) are combined measurements from multiple survey fields covering $\sim 12 \text{ deg}^2$, without accounting for variations in survey depth or differences in size cuts. Third, although the LAB sample at $z \sim 2.8$ reported by S. Kikuta et al. (2019) is close in redshift to this work ($z \sim 3.1$), their surface brightness depth is twice as deep as ODIN. We therefore also treat their measurement as an upper limit. Lastly, comparing higher-redshift LAB samples (T. Saito et al. 2006; T. Shibuya et al. 2018; H. Zhang et al. 2020) with our measurement is complex because the effects of flux boosting, shrinking sizes, and surface brightness depth must be considered simultaneously at the ODIN redshift ($z \sim 3.1$). Thus, we show their observed number densities as they are.

The LAB number density appears to peak around the Cosmic Noon ($z = 2\text{--}3$), mirroring the evolution of the cosmic star formation rate density (P. Madau & M. Dickinson 2014). T. Shibuya et al. (2018) interpreted a similar redshift trend as evidence that the origin of LABs is related to star formation. However, we note that it could also be associated with AGN activity, given the similar shape of the black hole accretion rate density evolution (e.g., F. Vito et al. 2018). A careful analysis of the redshift evolution of LABs, star formation, and AGN populations is therefore required to draw a firm conclusion.

The number density of ODIN LABs in proto-cluster regions (red dot) is consistent with that of the SSA22 LABs (black square), as well as with the upper limits

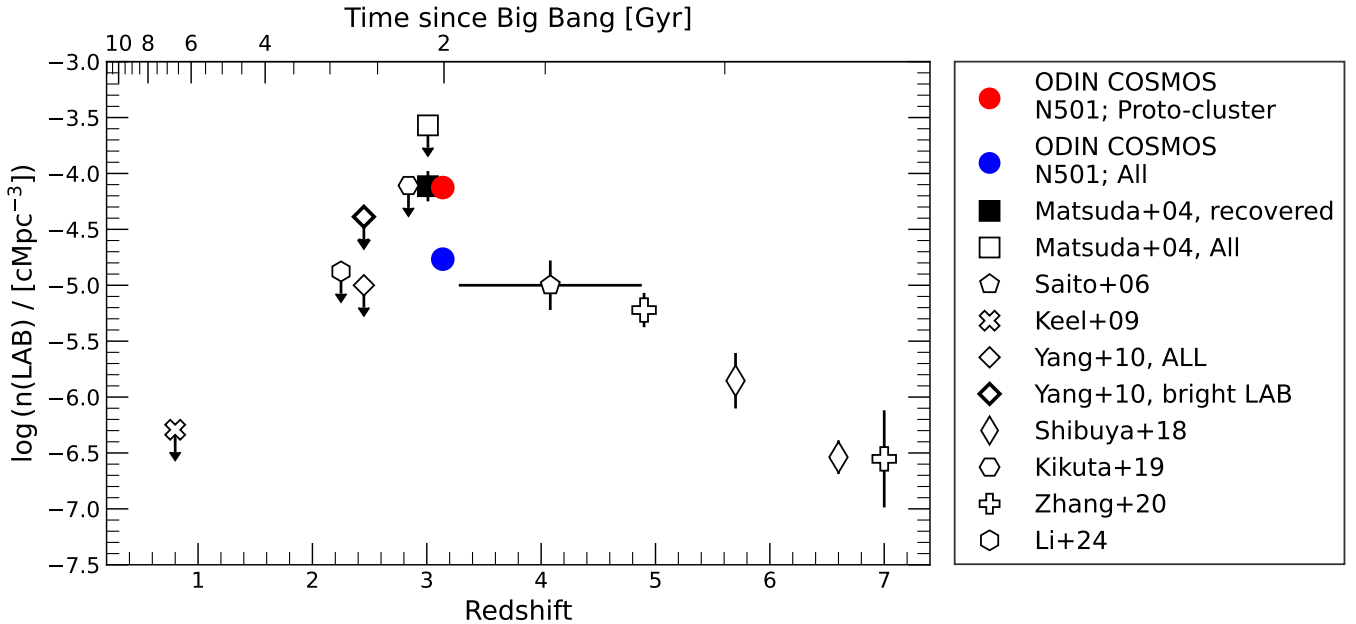


Figure 13. Number densities of LABs as a function of redshift (lower axis) and cosmic time (upper axis). Filled points indicate LAB samples whose number densities are directly comparable, while open points correspond to samples selected with different criteria and/or surface brightness depths, and are therefore treated as upper limits. The red circle represents the average number density at Complexes A and C. Some symbols are slightly shifted along the x -axis for clarity. The LAB number density appears to peak around Cosmic Noon ($z = 2-3$).

set by *S. Kikuta et al. (2019)*. The overall ODIN LAB sample (blue dot) is also consistent with the measurements at $z \sim 2.3$, while all cluster LAB number densities at $z \sim 3$ (COSMOS and SSA22) are higher than those at other redshifts, demonstrating that environmental effects must be carefully accounted for when constructing the number density evolution. To robustly trace the cosmic evolution of LABs, large-area surveys ($\gtrsim 10 \text{ deg}^2$), such as ODIN, with consistent sample selection across epochs, are essential.

5. SUMMARY

Using ODIN survey data in the E-COSMOS field, we identify a sample of 112 $z \sim 3.1$ Ly α blobs (LABs) with two complementary detection algorithms: one designed to find extended Ly α emission around LAEs (the extended LAE method), and the other newly developed to detect diffuse LABs using forced photometry with *Tractor*. These algorithms are being applied across the full $\sim 100 \text{ deg}^2$ ODIN survey in three different redshift windows.

Our principle findings in this paper are:

- We spectroscopically confirm five LAB candidates through our new Gemini/GMOS observations, and 47 additional LABs through the DESI DR1 spectra and the literature. This includes ten LABs identified by the new extended-beyond-continuum pipeline, further supporting the robustness and reliability of our LAB sample.

- We present measurements of the number density and the luminosity function of ODIN LABs. The number density of proto-cluster-associated LABs is higher than the ODIN LABs across the full E-COSMOS field. The luminosity function of the entire ODIN LABs is 1.5 times steeper than the proto-cluster-associated LABs. These results suggest the Ly α luminosities and number densities of LABs are environment-dependent. To robustly characterize the effect of environment, an even larger sample is required.
- The number density of LABs peaks around the Cosmic Noon ($z = 2-3$), mirroring the cosmic star formation and the black hole accretion rate histories. To robustly trace the cosmic evolution of LABs, ODIN-like surveys with large areas and consistent sample selection across epochs, are essential.

ACKNOWLEDGMENTS

Based on observations at Cerro Tololo Inter-American Observatory, NSF’s NOIRLab (Prop. ID 2020B-0201; PI: K.-S. Lee), which is managed by the Association of Universities for Research in Astronomy under a cooperative agreement with the National Science Foundation. We thank Yuichi Matsuda for providing the narrowband images of his Ly α blobs. BM and YY

are supported by the Basic Science Research Program through the National Research Foundation of Korea funded by the Ministry of Science, ICT & Future Planning (2019R1A2C4069803), and UST Young Scientist+ Research Program 2022 through the University of Science and Technology (2022YS45). KSL acknowledges financial support from the National Science Foundation under grant Nos. AST-2206705, AST-2408359, and from the Ross-Lynn Purdue Research Foundations. EG and NF acknowledge support from NSF grant AST-2206222. NF acknowledges support from NASA Astrophysics Data Analysis Program grant 80NSSC22K0487. This material is based upon work supported by the NSF Graduate Research Fellowship Program under Grant No. DGE-2233066 to NF. This work is supported by K-GMT Science Program (PID: GS-2021A-FT-211, GS-2021B-Q-110, GS-2023A-Q-110, GS-2025A-Q-110) of Korea Astronomy and Space Science Institute. The Institute for Gravitation and the Cosmos is supported by the Eberly College of Science

and the Office of the Senior Vice President for Research at the Pennsylvania State University. LG also gratefully acknowledges financial support from ANID-MILENIO-NCN2024.112, ANID BASAL project FB210003, and FONDECYT regular project number 1230591. HSH acknowledges the support of the National Research Foundation of Korea (NRF) grant funded by the Korea government (MSIT), NRF-2021R1A2C1094577, and Hyunsong Educational & Cultural Foundation. SL acknowledges support from the National Research Foundation of Korea (NRF) grant (Nos. RS-2025-00573214 and 2021M3F7A1084525) funded by the Korea government (MSIT).

Facilities: Blanco (DECam), Gemini:South (GMOS)

Software: Source Extractor (E. Bertin & S. Arnouts 1996), PSFEx (E. Bertin 2013), Tractor (D. Lang et al. 2016a), Astropy (Astropy Collaboration et al. 2013, 2018, 2022), Photutils (L. Bradley et al. 2025)

REFERENCES

- Aihara, H., AlSayyad, Y., Ando, M., et al. 2019, PASJ, 71, 114, doi: [10.1093/pasj/psj103](https://doi.org/10.1093/pasj/psj103)
- Ao, Y., Zheng, Z., Henkel, C., et al. 2020, Nature Astronomy, 4, 670, doi: [10.1038/s41550-020-1033-3](https://doi.org/10.1038/s41550-020-1033-3)
- Arrigoni Battaia, F., Prochaska, J. X., Hennawi, J. F., et al. 2018, MNRAS, 473, 3907, doi: [10.1093/mnras/stx2465](https://doi.org/10.1093/mnras/stx2465)
- Arrigoni Battaia, F., Chen, C.-C., Liu, H.-Y. B., et al. 2022, ApJ, 930, 72, doi: [10.3847/1538-4357/ac5a4d](https://doi.org/10.3847/1538-4357/ac5a4d)
- Astropy Collaboration, Robitaille, T. P., Tollerud, E. J., et al. 2013, A&A, 558, A33, doi: [10.1051/0004-6361/201322068](https://doi.org/10.1051/0004-6361/201322068)
- Astropy Collaboration, Price-Whelan, A. M., Sipőcz, B. M., et al. 2018, AJ, 156, 123, doi: [10.3847/1538-3881/aabc4f](https://doi.org/10.3847/1538-3881/aabc4f)
- Astropy Collaboration, Price-Whelan, A. M., Lim, P. L., et al. 2022, ApJ, 935, 167, doi: [10.3847/1538-4357/ac7c74](https://doi.org/10.3847/1538-4357/ac7c74)
- Bertin, E. 2013, PSFEx: Point Spread Function Extractor,, Astrophysics Source Code Library, record ascl:1301.001 <http://ascl.net/1301.001>
- Bertin, E., & Arnouts, S. 1996, A&AS, 117, 393, doi: [10.1051/aas:1996164](https://doi.org/10.1051/aas:1996164)
- Bradley, L., Sipőcz, B., Robitaille, T., et al. 2025, astropy/photutils: 2.2.0, 2.2.0 Zenodo, doi: [10.5281/zenodo.14889440](https://doi.org/10.5281/zenodo.14889440)
- Bădescu, T., Yang, Y., Bertoldi, F., et al. 2017, ApJ, 845, 172, doi: [10.3847/1538-4357/aa8220](https://doi.org/10.3847/1538-4357/aa8220)
- Cai, Z., Fan, X., Yang, Y., et al. 2017, ApJ, 837, 71, doi: [10.3847/1538-4357/aa5d14](https://doi.org/10.3847/1538-4357/aa5d14)
- Cantalupo, S., Arrigoni-Battaia, F., Prochaska, J. X., Hennawi, J. F., & Madau, P. 2014, Nature, 506, 63, doi: [10.1038/nature12898](https://doi.org/10.1038/nature12898)
- Chang, S.-J., Yang, Y., Seon, K.-I., Zabludoff, A., & Lee, H.-W. 2023, ApJ, 945, 100, doi: [10.3847/1538-4357/acac98](https://doi.org/10.3847/1538-4357/acac98)
- Cool, R. J., Moustakas, J., Blanton, M. R., et al. 2013, ApJ, 767, 118, doi: [10.1088/0004-637X/767/2/118](https://doi.org/10.1088/0004-637X/767/2/118)
- Daddi, E., Valentino, F., Rich, R. M., et al. 2021, A&A, 649, A78, doi: [10.1051/0004-6361/202038700](https://doi.org/10.1051/0004-6361/202038700)
- Daddi, E., Rich, R. M., Valentino, F., et al. 2022, ApJL, 926, L21, doi: [10.3847/2041-8213/ac531f](https://doi.org/10.3847/2041-8213/ac531f)
- de Vaucouleurs, G. 1948, Annales d’Astrophysique, 11, 247
- DESI Collaboration, Abdul-Karim, M., Adame, A. G., et al. 2025, arXiv e-prints, arXiv:2503.14745, doi: [10.48550/arXiv.2503.14745](https://doi.org/10.48550/arXiv.2503.14745)
- Dey, A., Bian, C., Soifer, B. T., et al. 2005, ApJ, 629, 654, doi: [10.1086/430775](https://doi.org/10.1086/430775)
- Dey, A., Schlegel, D. J., Lang, D., et al. 2019, AJ, 157, 168, doi: [10.3847/1538-3881/ab089d](https://doi.org/10.3847/1538-3881/ab089d)
- Erb, D. K., Bogosavljević, M., & Steidel, C. C. 2011, ApJL, 740, L31, doi: [10.1088/2041-8205/740/1/L31](https://doi.org/10.1088/2041-8205/740/1/L31)
- Firestone, N. M., Gawiser, E., Ramakrishnan, V., et al. 2024, ApJ, 974, 217, doi: [10.3847/1538-4357/ad71c9](https://doi.org/10.3847/1538-4357/ad71c9)
- Flaugher, B., Diehl, H. T., Honscheid, K., et al. 2015, AJ, 150, 150, doi: [10.1088/0004-6256/150/5/150](https://doi.org/10.1088/0004-6256/150/5/150)
- Francis, P. J., Williger, G. M., Collins, N. R., et al. 2001, ApJ, 554, 1001, doi: [10.1086/321417](https://doi.org/10.1086/321417)

- Geach, J. E., Alexander, D. M., Lehmer, B. D., et al. 2009, *ApJ*, 700, 1, doi: [10.1088/0004-637X/700/1/1](https://doi.org/10.1088/0004-637X/700/1/1)
- Geach, J. E., Narayanan, D., Matsuda, Y., et al. 2016, *ApJ*, 832, 37, doi: [10.3847/0004-637X/832/1/37](https://doi.org/10.3847/0004-637X/832/1/37)
- Gronke, M. 2017, *A&A*, 608, A139, doi: [10.1051/0004-6361/201731791](https://doi.org/10.1051/0004-6361/201731791)
- Hasinger, G., Capak, P., Salvato, M., et al. 2018, *ApJ*, 858, 77, doi: [10.3847/1538-4357/aabacf](https://doi.org/10.3847/1538-4357/aabacf)
- Hayes, M., Scarlata, C., & Siana, B. 2011, *Nature*, 476, 304, doi: [10.1038/nature10320](https://doi.org/10.1038/nature10320)
- Hennawi, J. F., Prochaska, J. X., Cantalupo, S., & Arrigoni-Battaia, F. 2015, *Science*, 348, 779, doi: [10.1126/science.aaa5397](https://doi.org/10.1126/science.aaa5397)
- Herrera, D., Gawiser, E., Benda, B., et al. 2025, *ApJL*, 988, L57, doi: [10.3847/2041-8213/adec82](https://doi.org/10.3847/2041-8213/adec82)
- Hill, G. J., Lee, H., MacQueen, P. J., et al. 2021, *AJ*, 162, 298, doi: [10.3847/1538-3881/ac2c02](https://doi.org/10.3847/1538-3881/ac2c02)
- Hogg, D. W. 2008, arXiv e-prints, arXiv:0807.4820, doi: [10.48550/arXiv.0807.4820](https://doi.org/10.48550/arXiv.0807.4820)
- Hong, S., Dey, A., Lee, K.-S., et al. 2019, *MNRAS*, 483, 3950, doi: [10.1093/mnras/sty3219](https://doi.org/10.1093/mnras/sty3219)
- Hook, I. M., Jørgensen, I., Allington-Smith, J. R., et al. 2004, *PASP*, 116, 425, doi: [10.1086/383624](https://doi.org/10.1086/383624)
- Kato, Y., Matsuda, Y., Iono, D., et al. 2018, *PASJ*, 70, L6, doi: [10.1093/pasj/psy087](https://doi.org/10.1093/pasj/psy087)
- Keel, W. C., Cohen, S. H., Windhorst, R. A., & Waddington, I. 1999, *AJ*, 118, 2547, doi: [10.1086/301139](https://doi.org/10.1086/301139)
- Keel, W. C., White, Raymond E., I., Chapman, S., & Windhorst, R. A. 2009, *AJ*, 138, 986, doi: [10.1088/0004-6256/138/3/986](https://doi.org/10.1088/0004-6256/138/3/986)
- Kikuta, S., Matsuda, Y., Cen, R., et al. 2019, *PASJ*, 71, L2, doi: [10.1093/pasj/psz055](https://doi.org/10.1093/pasj/psz055)
- Kim, E., Yang, Y., Zabludoff, A., et al. 2020, *ApJ*, 894, 33, doi: [10.3847/1538-4357/ab837f](https://doi.org/10.3847/1538-4357/ab837f)
- Kriek, M., van Dokkum, P. G., Franx, M., et al. 2007, *ApJ*, 669, 776, doi: [10.1086/520789](https://doi.org/10.1086/520789)
- Kusakabe, H., Verhamme, A., Blaizot, J., et al. 2022, *A&A*, 660, A44, doi: [10.1051/0004-6361/202142302](https://doi.org/10.1051/0004-6361/202142302)
- Lang, D., Hogg, D. W., & Mykytyn, D. 2016a, *The Tractor: Probabilistic astronomical source detection and measurement*, Astrophysics Source Code Library, record ascl:1604.008 <http://ascl.net/1604.008>
- Lang, D., Hogg, D. W., & Schlegel, D. J. 2016b, *AJ*, 151, 36, doi: [10.3847/0004-6256/151/2/36](https://doi.org/10.3847/0004-6256/151/2/36)
- Langen, V., Cantalupo, S., Steidel, C. C., et al. 2023, *MNRAS*, 519, 5099, doi: [10.1093/mnras/stac3205](https://doi.org/10.1093/mnras/stac3205)
- Leclercq, F., Bacon, R., Wisotzki, L., et al. 2017, *A&A*, 608, A8, doi: [10.1051/0004-6361/201731480](https://doi.org/10.1051/0004-6361/201731480)
- Lee, K.-S., Gawiser, E., Park, C., et al. 2024, *ApJ*, 962, 36, doi: [10.3847/1538-4357/ad165e](https://doi.org/10.3847/1538-4357/ad165e)
- Li, M., Zhang, H., Cai, Z., et al. 2024, *ApJS*, 275, 27, doi: [10.3847/1538-4365/ad812c](https://doi.org/10.3847/1538-4365/ad812c)
- Lilly, S. J., Le Brun, V., Maier, C., et al. 2009, *ApJS*, 184, 218, doi: [10.1088/0067-0049/184/2/218](https://doi.org/10.1088/0067-0049/184/2/218)
- Lusso, E., Fumagalli, M., Fossati, M., et al. 2019, *MNRAS*, 485, L62, doi: [10.1093/mnras/slz032](https://doi.org/10.1093/mnras/slz032)
- Madau, P., & Dickinson, M. 2014, *ARA&A*, 52, 415, doi: [10.1146/annurev-astro-081811-125615](https://doi.org/10.1146/annurev-astro-081811-125615)
- Matsuda, Y., Yamada, T., Hayashino, T., et al. 2004, *AJ*, 128, 569, doi: [10.1086/422020](https://doi.org/10.1086/422020)
- Matsuda, Y., Yamada, T., Hayashino, T., et al. 2011, *MNRAS*, 410, L13, doi: [10.1111/j.1745-3933.2010.00969.x](https://doi.org/10.1111/j.1745-3933.2010.00969.x)
- Momcheva, I. G., Brammer, G. B., van Dokkum, P. G., et al. 2016, *ApJS*, 225, 27, doi: [10.3847/0067-0049/225/2/27](https://doi.org/10.3847/0067-0049/225/2/27)
- Momose, R., Ouchi, M., Nakajima, K., et al. 2016, *MNRAS*, 457, 2318, doi: [10.1093/mnras/stw021](https://doi.org/10.1093/mnras/stw021)
- Nagaraj, G., Ciardullo, R., Gronwall, C., et al. 2025, arXiv e-prints, arXiv:2506.14510, doi: [10.48550/arXiv.2506.14510](https://doi.org/10.48550/arXiv.2506.14510)
- Ouchi, M., Ono, Y., & Shibuya, T. 2020, *ARA&A*, 58, 617, doi: [10.1146/annurev-astro-032620-021859](https://doi.org/10.1146/annurev-astro-032620-021859)
- Ouchi, M., Ono, Y., Egami, E., et al. 2009, *ApJ*, 696, 1164, doi: [10.1088/0004-637X/696/2/1164](https://doi.org/10.1088/0004-637X/696/2/1164)
- Palunas, P., Teplitz, H. I., Francis, P. J., Williger, G. M., & Woodgate, B. E. 2004, *ApJ*, 602, 545, doi: [10.1086/381145](https://doi.org/10.1086/381145)
- Pâris, I., Petitjean, P., Aubourg, É., et al. 2014, *A&A*, 563, A54, doi: [10.1051/0004-6361/201322691](https://doi.org/10.1051/0004-6361/201322691)
- Prescott, M. K. M., Dey, A., & Jannuzi, B. T. 2012a, *ApJ*, 748, 125, doi: [10.1088/0004-637X/748/2/125](https://doi.org/10.1088/0004-637X/748/2/125)
- Prescott, M. K. M., Kashikawa, N., Dey, A., & Matsuda, Y. 2008, *ApJL*, 678, L77, doi: [10.1086/588606](https://doi.org/10.1086/588606)
- Prescott, M. K. M., Dey, A., Brodwin, M., et al. 2012b, *ApJ*, 752, 86, doi: [10.1088/0004-637X/752/2/86](https://doi.org/10.1088/0004-637X/752/2/86)
- Ramakrishnan, V., Moon, B., Im, S. H., et al. 2023, *ApJ*, 951, 119, doi: [10.3847/1538-4357/acd341](https://doi.org/10.3847/1538-4357/acd341)
- Ramakrishnan, V., Lee, K.-S., Artale, M. C., et al. 2024, *ApJ*, 977, 119, doi: [10.3847/1538-4357/ad83cb](https://doi.org/10.3847/1538-4357/ad83cb)
- Ramakrishnan, V., Ortiz, A., Moon, B., et al. 2025a, arXiv e-prints, arXiv:2511.11826, doi: [10.48550/arXiv.2511.11826](https://doi.org/10.48550/arXiv.2511.11826)
- Ramakrishnan, V., Lee, K.-S., Firestone, N., et al. 2025b, *ApJ*, 982, 74, doi: [10.3847/1538-4357/adb624](https://doi.org/10.3847/1538-4357/adb624)
- Rosdahl, J., & Blaizot, J. 2012, *MNRAS*, 423, 344, doi: [10.1111/j.1365-2966.2012.20883.x](https://doi.org/10.1111/j.1365-2966.2012.20883.x)
- Saito, T., Shimasaku, K., Okamura, S., et al. 2006, *ApJ*, 648, 54, doi: [10.1086/505678](https://doi.org/10.1086/505678)
- Sérsic, J. L. 1963, *Boletín de la Asociación Argentina de Astronomía La Plata Argentina*, 6, 41

- Shibuya, T., Ouchi, M., Konno, A., et al. 2018, PASJ, 70, S14, doi: [10.1093/pasj/psx122](https://doi.org/10.1093/pasj/psx122)
- Silverman, J. D., Kashino, D., Sanders, D., et al. 2015, ApJS, 220, 12, doi: [10.1088/0067-0049/220/1/12](https://doi.org/10.1088/0067-0049/220/1/12)
- Smith, D. J. B., & Jarvis, M. J. 2007, MNRAS, 378, L49, doi: [10.1111/j.1745-3933.2007.00318.x](https://doi.org/10.1111/j.1745-3933.2007.00318.x)
- Steidel, C. C., Adelberger, K. L., Shapley, A. E., et al. 2000, ApJ, 532, 170, doi: [10.1086/308568](https://doi.org/10.1086/308568)
- Tornotti, D., Fumagalli, M., Fossati, M., et al. 2025, Nature Astronomy, 9, 577, doi: [10.1038/s41550-024-02463-w](https://doi.org/10.1038/s41550-024-02463-w)
- Umeda, H., Ouchi, M., Kikuta, S., et al. 2025, ApJS, 277, 37, doi: [10.3847/1538-4365/adb1c0](https://doi.org/10.3847/1538-4365/adb1c0)
- Umehata, H., Fumagalli, M., Smail, I., et al. 2019, Science, 366, 97, doi: [10.1126/science.aaw5949](https://doi.org/10.1126/science.aaw5949)
- Vito, F., Brandt, W. N., Yang, G., et al. 2018, MNRAS, 473, 2378, doi: [10.1093/mnras/stx2486](https://doi.org/10.1093/mnras/stx2486)
- Yamada, T., Matsuda, Y., Kousai, K., et al. 2012, ApJ, 751, 29, doi: [10.1088/0004-637X/751/1/29](https://doi.org/10.1088/0004-637X/751/1/29)
- Yang, Y., Zabludoff, A., Eisenstein, D., & Davé, R. 2010, ApJ, 719, 1654, doi: [10.1088/0004-637X/719/2/1654](https://doi.org/10.1088/0004-637X/719/2/1654)
- Yang, Y., Zabludoff, A., Jahnke, K., & Davé, R. 2014, ApJ, 793, 114, doi: [10.1088/0004-637X/793/2/114](https://doi.org/10.1088/0004-637X/793/2/114)
- Yang, Y., Zabludoff, A., Jahnke, K., et al. 2011, ApJ, 735, 87, doi: [10.1088/0004-637X/735/2/87](https://doi.org/10.1088/0004-637X/735/2/87)
- Yang, Y., Zabludoff, A., Tremonti, C., Eisenstein, D., & Davé, R. 2009, ApJ, 693, 1579, doi: [10.1088/0004-637X/693/2/1579](https://doi.org/10.1088/0004-637X/693/2/1579)
- You, C., Zabludoff, A., Smith, P., et al. 2017, ApJ, 834, 182, doi: [10.3847/1538-4357/834/2/182](https://doi.org/10.3847/1538-4357/834/2/182)
- Zhang, H., Ouchi, M., Itoh, R., et al. 2020, ApJ, 891, 177, doi: [10.3847/1538-4357/ab7917](https://doi.org/10.3847/1538-4357/ab7917)
- Zhang, H., Cai, Z., Li, M., et al. 2025, ApJ, 981, 70, doi: [10.3847/1538-4357/adb41b](https://doi.org/10.3847/1538-4357/adb41b)

APPENDIX

A. SURFACE BRIGHTNESS PROFILE OF LABS AND LAES

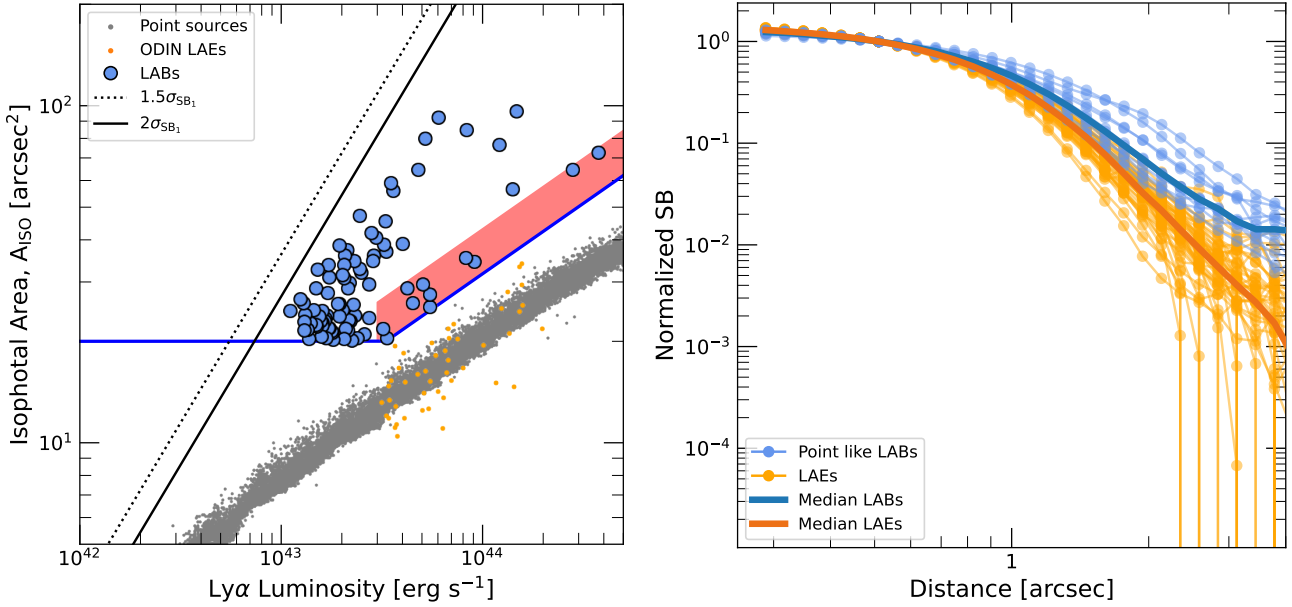


Figure A1. **Left:** The blue circles represent the 89 LAB candidates selected using the extended-LAE method; the red shaded region indicates LABs near the point-source size–luminosity relation. The LABs closest to the point-source luminosity–size relation (defined as those within the 3σ – 5σ scatter estimated for point sources with Ly α luminosity 3×10^{43} erg s $^{-1}$) are highlighted in the red-shaded region. The ODIN LAEs used in the comparison are shown as orange dots and also have Ly α luminosities above 3×10^{43} erg s $^{-1}$. **Right:** Surface brightness profiles of LABs and LAEs at $0.5''$, corresponding to the half of the seeing in the $N501$ band. The bordered lines indicates median of the 1D profiles. LABs (blue solid line and circles) exhibit more spatially extended profiles than LAEs (orange solid line and circles), indicating that LABs near the point-source branch are indeed more extended than LAEs with comparable Ly α luminosities.

To confirm the nature of LAB candidates near the size-luminosity relation of simulated point sources, we compare their surface brightness profiles with those of LAEs. Specifically, we select LABs that lie within 5σ of the size–luminosity relation of the simulated point sources and have Ly α luminosities above 3×10^{43} erg s $^{-1}$ (Figure A1, left). For comparison, we use the independently identified LAEs within the same luminosity range. These selections yield 11 LAB candidates above the point-source relation and 47 LAEs lying along the relation.

We extract surface brightness profiles from both LABs and LAEs using *Ellipse* in Python *Photutils* package. Each profile is normalized to the surface brightness at $0.5''$, which corresponds to the half of seeing in the $N501$ band. Figure A1 (right) shows that the profiles of LAB candidates are more spatially extended than LAEs, indicating that LABs near the point-source branch are indeed more extended than LAEs with similar luminosities. These different profiles support the classification of these LABs as genuinely extended sources, despite their proximity to the point-source relation in the size–luminosity space.

B. LAB CATALOG

Table B1. ODIN LAB Catalog

Name	R.A.	Decl.	$L(\text{Ly}\alpha)$	A_{iso}^1	Ly α Size	f_{recy}	LAB Selection				Redshift	Note
							deg	deg	$10^{43} \text{ erg s}^{-1}$	arcsec ²		
ODIN-COSMOS-z3p1-LAB001	151.791042	2.873806	37.41 \pm 0.24	72.2 \pm 18.2	185	1.000	Y
ODIN-COSMOS-z3p1-LAB002	151.073375	2.225167	27.90 \pm 0.14	64.5 \pm 6.9	107	1.000	Y	Y	Y	DESI
ODIN-COSMOS-z3p1-LAB003	151.041375	2.513778	14.73 \pm 0.17	95.7 \pm 7.9	110	1.000	Y	Y	Y	3.1324	3.1324	R25
ODIN-COSMOS-z3p1-LAB004	148.726667	2.786306	14.07 \pm 0.15	56.3 \pm 7.8	102	1.000	Y	Y	Y	3.0825	3.0825	This work,SDSS-DR14Q,DESI
ODIN-COSMOS-z3p1-LAB005	150.474375	3.068111	12.06 \pm 0.16	76.1 \pm 8.6	99	1.000	Y	Y	Y
ODIN-COSMOS-z3p1-LAB006	149.489417	3.582750	9.11 \pm 0.12	34.4 \pm 5.9	76	0.979	Y	Y	Y
ODIN-COSMOS-z3p1-LAB007	150.619958	2.671500	8.31 \pm 0.16	84.6 \pm 12.4	108	1.000	Y	Y	Y	3.1493	3.1493	PRIMUS,ZCOSMOS,R25
ODIN-COSMOS-z3p1-LAB008	149.085250	2.535417	8.28 \pm 0.11	35.4 \pm 6.0	81	0.993	Y	Y	Y	DESI
ODIN-COSMOS-z3p1-LAB009	148.972500	1.593694	6.01 \pm 0.17	92.0 \pm 21.6	152	1.000	Y	Y	Y
ODIN-COSMOS-z3p1-LAB010	150.764458	3.091083	5.49 \pm 0.09	25.2 \pm 3.8	62	0.858	Y	Y	Y	DESI
ODIN-COSMOS-z3p1-LAB011	149.274458	1.165694	5.45 \pm 0.09	27.4 \pm 8.5	63	0.930	Y	3.1066	3.1066	SDSS-DR14Q,DESI
ODIN-COSMOS-z3p1-LAB012	148.848917	2.638417	5.21 \pm 0.16	79.8 \pm 10.4	103	1.000	Y	Y	Y	3.1189	3.1189	This work
ODIN-COSMOS-z3p1-LAB013	149.497875	0.735222	5.04 \pm 0.12	29.4 \pm 3.9	73	0.995	Y	Y	Y	DESI
ODIN-COSMOS-z3p1-LAB014	149.452250	1.667333	4.77 \pm 0.15	64.5 \pm 15.7	108	1.000	Y	3.1326 ²	3.1326 ²	This work
ODIN-COSMOS-z3p1-LAB015	148.857625	2.136722	4.50 \pm 0.12	25.9 \pm 7.4	64	0.921	Y	DESI
ODIN-COSMOS-z3p1-LAB016	150.489833	1.148167	4.23 \pm 0.09	28.7 \pm 3.5	59	1.000	Y	Y	Y
ODIN-COSMOS-z3p1-LAB017	149.969250	2.304861	4.00 \pm 0.12	38.9 \pm 5.6	69	1.000	Y	Y	Y	3.15	3.15	DEIMOS 10k
ODIN-COSMOS-z3p1-LAB018	149.704083	2.657806	3.61 \pm 0.14	55.9 \pm 8.5	100	1.000	Y	Y	Y	3.1335	3.1335	This work,DESI
ODIN-COSMOS-z3p1-LAB019	149.240000	2.479167	3.51 \pm 0.14	58.8 \pm 7.7	92	1.000	Y	Y	Y
ODIN-COSMOS-z3p1-LAB020	151.733208	3.074139	3.35 \pm 0.12	20.4 \pm 4.2	61	0.855	Y	Y	Y

NOTE— Column (1) LAB ID, (2)–(3) coordinates, (4) Ly α luminosity, (5) isophotal size, (6) projected end-to-end Ly α extent (7) recovery fraction from Section 3.4, (8)–(9) whether each LAB is identified by extended-LAE and/or extended-beyond-continuum methods, (10) spectroscopic redshift, (11) notes and source of the spectroscopic confirmation. ‘‘R25’’ indicates Keck/DEIMOS observations from V. Ramakrishnan et al. (2025a). The ‘‘DESI’’ tag indicates DESI DR1 spectra (DESI Collaboration et al. 2025). Only the first 20 sources are listed.

¹ The uncertainty of Ly α size is defined as the standard deviation of the recovered Ly α sizes from the recovery test (Section 3.4).

² The peak of Ly α emission coincided with a bad column (Figure 9).